MASTER'S THESIS

Master Nanotechnologies for ICT
2020

Capacitive CMOS compatible transducer design for particulate matter sensor

Author: **Lucas Reganaz**

Email: lucas.reganaz@grenoble-inp.org

Supervisors: Oleg Sakolski (Fraunhofer, EMFT)

Youla Morfouli (Grenoble INP - Phelma)

Begin: February 17, 2020

End: August 14, 2020

Abstract

Airborne Particulate Matter (PM) capacitive sensing is a challenging technology. But the on-chip integration of such a sensor would allow a cheaper, efficient but most of all embeddable sensing solution. PM capacitive sensing can be performed with an interdigitated capacitor (IDC) structure. Such design has been widely described and several analytical models to describe their electrical and capacitive behavior already exist. This work aims at developing an analytical model for the capacitance response of an IDC to a PM. This model has shown a very good accuracy compared to FEM simulation, especially for small particles compared to the size of an electrode from the IDC. The limitations of the model are also well defined and described.

Abstract

Le capteur capacitif pour particules en suspension dans l'air (PM) est une technologie difficile à mettre en oeuvre. Cependant, l'intégration sur puce électronique d'un tel capteur débloquerait une solution peu cher, efficace mais avant tout facilement intégrable. La détection capacitive de PM peut être réalisée par capacitances interdigitalisées (IDC). Cette structure a été largement étudiée et il existe déjà plusieurs modèles analytiques pour en décrire le comportement électrique et capacitif. Ce travail vise à développer un model analytique pour la réponse en capacitance de la structure IDC en présence de particules. Ce modèle a montré une très bonne précision de résultat comparé à la simulation à élément finis FEM, en particulier pour de petites tailles de particules devant la taille des électrodes de l'IDC. Les limitations du modèle sont égalament bien définies et décrites.

Descritto

Il rilevamento capacitivo di particolato atmosferico (PM) è una tecnologia impegnativa. Ma l'integrazione su chip di un tale sensore consentirebbe una soluzione di rilevamento più economica, efficiente ma soprattutto integrabile. Il rilevamento capacitivo del PM può essere eseguito con una struttura a condensatore interdigitato (IDC). Tale progettazione è stata ampiamente descritta ed esistono già diversi modelli analitici per descrivere il loro comportamento elettrico e capacitivo. Questo lavoro mira a sviluppare un modello analitico per la risposta capacitiva di un IDC a un PM. Questo modello ha mostrato una precisione molto buona rispetto alla simulazione FEM, soprattutto per particelle piccole rispetto alle dimensioni di un elettrodo dell'IDC. Anche i limiti del modello sono ben definiti e descritti.

Contents

List of Abbreviations

CM	Conformal mapping
CMOS	Complementary metal-oxide-semiconductor
CPW	Coplanar waveguide
DB	Dirichlet boundary
EFD	Electric field density
FEM	Finite element method
IDC	Interdigital capacitor
MEMS	Micro-electro-mechanical system
MOS	Metal-oxide-semiconductor
NB	Neumann boundary
PM	Particulate matter
QCM	Quartz-crystal microbalance
SEM	scanning electron microscopy
SoC	Silicon on Chip
TFBAR	Thin film bulk acoustic resonator
THR	Transparent heat reflector

List of Symbols

ΔC	Absolute capacitance increment due to particle
δC	Relative capacitance increment due to particle
δD	Relative EFD increment due to particle
ϵ_0	Vacuum permittivity
η	Metalization ratio
λ	Interdigital electrodes spatial wavelength
$\overline{\boldsymbol{D'}}$	EFD distortion average over any ellipsoid orientation
$\overline{\boldsymbol{D'_\infty}}$	EFD distortion average over any metallic ellipsoid orientation
$\boldsymbol{A}$	Ellipsoid shape factor matrix
$\boldsymbol{D'}$	EFD distortion nearby a particle
$\boldsymbol{D_0}$	Initial electric field density
$\boldsymbol{D_p}$	EFD inside a particle
$\boldsymbol{D'_\infty}$	EFD distortion nearby a metallic particle
$\boldsymbol{D_{air}}$	EFD in the air outside a particle
$\boldsymbol{D}$	EFD with particle
$\boldsymbol{E_0}$	Initial electric field
$\boldsymbol{K}$	Ellipsoid demagnetizing factor matrix
a, b, c	Ellipsoid parameters
A_i	Ellipsoid shape factor with respect to parameter i
C	IDC capacitance with particle
$C0$	IDC capacitance
C_E	Exterior capacitance
C_I	Interior capacitance
e	Ellipsoid parameter defined as a/c
$E(\varphi,k)$	Incomplete elliptic integral of second kind of amplitude φ and modulus k
$F(\varphi,k)$	Incomplete elliptic integral of first kind of amplitude φ and modulus k
G	Gap between electrodes
g	Ellipsoid parameter defined as b/c

h	Thickness of a dielectric layer
k	Volume fraction of the ellipsoid
$K(k)$	Complete elliptic integral of first kind of modulus k
L	Effective interdigital length
L_i	Ellipsoid depolarization factor with respect to parameter i
N	IDC number of fingers
q	Distributed electric charge over the mapped plate
q	Electric charge density in the mapped plate
r	Ratio between dielectric layer thickness and spatial wavelength
S	Surface area of the mapped parallel plate capacitor
t	Fingers thickness
U	Electric potential difference of the mapped parallel plate
W	Finger width

Introduction

Air and atmospheric pollution monitoring technologies have been developed over the last few decades. It has enabled the detection of a wide range of pollutants including mainly gas and particles. The large variety of pollutants makes air pollution monitoring more complex. In order to evaluate the air pollution monitoring efficiency, one has to consider, on the one hand, the sensitivity and the selectivity of the sensing station to the said pollutant. In other words, the monitoring sensor must respond to the concentration range of pollutant for which it has been designed. The selectivity is also important since all compounds don't have equal properties and it is often required to analyse or detect them independently. On the other hand, one requires the monitored areas to be finely mapped. Indeed, the finer the mapping, the easier the pollution source can be identified. Besides, it also increases the monitoring resolution and thus the absolute quantitative measurement over an area. For a long time, the solutions deployed for airborne particle detection were stationary, bulky and very expensive, namely because of the maintenance it requires. But air pollution monitoring has a changing paradigm due to portable and lower-cost sensor current development [1].

A wide range of technologies are used for gaseous mixture sensing (MOS sensor, infrared point or imaging, photoionozation, ...). The MOS sensor is namely an excellent candidate for low concentration gas sensing applications (even below ppm level), with an obvious ease of integrability thanks to MOS compatibility [2]. However, particulate matter (PM) sensing remains more challenging to include both sensing efficiency and device portability. The most common PM sensing technique is using light scattering and can now be embedded in a device that fits in the palm of a hand (SPS30 from Sensirion AG Switzerland or HPM series from Honeywell International INC.). But designing a sensor that is compatible with a wireless sensor network (IoT) requires to push even further the downsizing and the integrability. Such a device must be cheap and easily embedded. Developing this application could unlock low consumption device solutions and address the issue of the area monitoring fineness. Among few technologies for PM sensing, capacitive transducer is a good candidate for a on-chip transducer.

The objective of this work is to develop and characterize a MOS compatible and highly sensitive capacitive on-chip PM sensor. This report aims to provide a good understanding of the specifications a PM sensor must meet. This work focuses on developing an analytical physical description of the capacitive transducing part. Some trade-offs upon the device characteristics and parameters will be discussed.

In a first part, PM will be described as well as sensing technologies, namely capacitive, object of this work. In a second part, a complete analytical description will be made on the IDC capacitive transducer. In the third part, the already existing analytical model for IDC capacitance will be completed with a new approach to determine the capacitance effect of PM on the IDC. Last, some experimental characterization of IDC structures will be performed and discussed.

1 Particulate Matter IDC Sensor

In this chapter, an interdigital capacitor (IDC) for particulate matter sensing will be presented. An introduction will be given first on the effects of the particulate matter to the environment and to health, as well as its composition and what are the multiple sources. In the second part, PM monitoring technologies will be presented as well as the regulations that are set worldwide. Finally, the working principle of the IDC for capacitive PM sensing will be described.

1.1 PM : Effects, composition and sources

Air pollution is a major component of the global climate change. While the effect of greenhouse gases is known with a relative high accuracy, PM's climate effect remains quite uncertain. Yet it has been shown that aerosols can reduce significantly solar radiations with a negative net radiative forcing [3]. However, its impact on health is indisputable. As illustrated in Fig.1.1, particles smaller than 10 µm (the size refers to an aerodynamic diameter) go deep in the respiratory tract (they are not filtered in the nose nor the throat). PM are usually classified in three different categories regarding their size: (i) the inhalable are the particles with a size smaller than 10 µm (PM_{10}); (ii) the thoracic particles ($PM_{2.5}$), smaller than 2.5 µm, rest deeper in the bronchioles; (iii) ultra fine particles ($PM_{0.1}$), smaller than 0.1 µm, are considered as respiratory particles and can reach the circulatory system [4]. The absorption in the body of such chemicals causes many respiratory issues and health hazards in general [5]–[8]. In 2013, the ESCAPE study showed that there is no particulate concentration level that is safe: every increase of $10\,\mu g\,m^{-3}$ of PM_{10} and $PM_{2.5}$ make the lung cancer rate raise by 22% and 36%, respectively [9].

As mentioned previously, the effect that PM have on health depends on the size. But the chemical composition has also an important impact, namely once the said particle enters the circulatory system of the body and interacts with organs. Particulate matters are mainly composed of soil dust, sea salt, carbonaceous aerosols (organic and black carbon) or biogenic aerosols [10]. The toxicity of the particles is well documented [11] and for instance, soil dust and salts, which are mainly natural, are not as hazardous as some other compounds like transition metals, used in many industries.

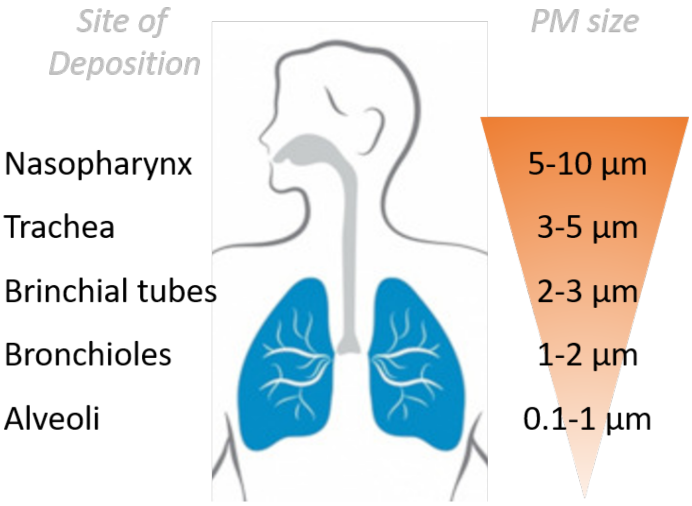

Figure 1.1: PM penetration depth in the respiratory system with respect to the size.

These various compositions and forms are in fact directly related to their sources, natural or anthropogenic. In order to give a good understanding of the different airborne particles sources, Kundu and Stone have studied in [12] the composition and sources of PM across Iowa, including rural and urban areas, as well as industrial and non-industrial sites. Unsurprisingly, it reveals that industrial sites and gas/diesel combustion are two important sources of PM_{10} and $PM_{2.5}$.

1.2 Regulations and monitoring technologies

In order to limit PM emissions worldwide, some countries have set their own emission regulations. Some of these regulations are displayed in table 1.1. In order to perform air quality monitoring, sensors are placed around potential sources of PM emission, basically around urban areas. These sensors need to analyse 2 parameters: the size of each particle and the corresponding concentration for this PM size class, measured as a volumetric mass density, usually in $\mu g/m^3$. The importance of size distribution analysis is that ultra fine particles often account for a few percentage of the total mass of particles in a same volume, but for about 90% of the number [13].

The most used technique remains laser scattering. This is one of the few methods that allow granulometric spectro-analysis (Concentration and size distribution analysis). The working principle is the following: A laser beam is emitted and goes through a volume of air containing a certain concentration and size distribution of PM. A part of the light is transmitted and the rest is deflected or scattered. This principle is based on the theory of Mie scattering, a solution to Maxwell's equations for an electromagnetic wave scattered by a sphere [14]. This is an efficient method that does not depend on the chemical composition of the particles but only on the concentration and the size.

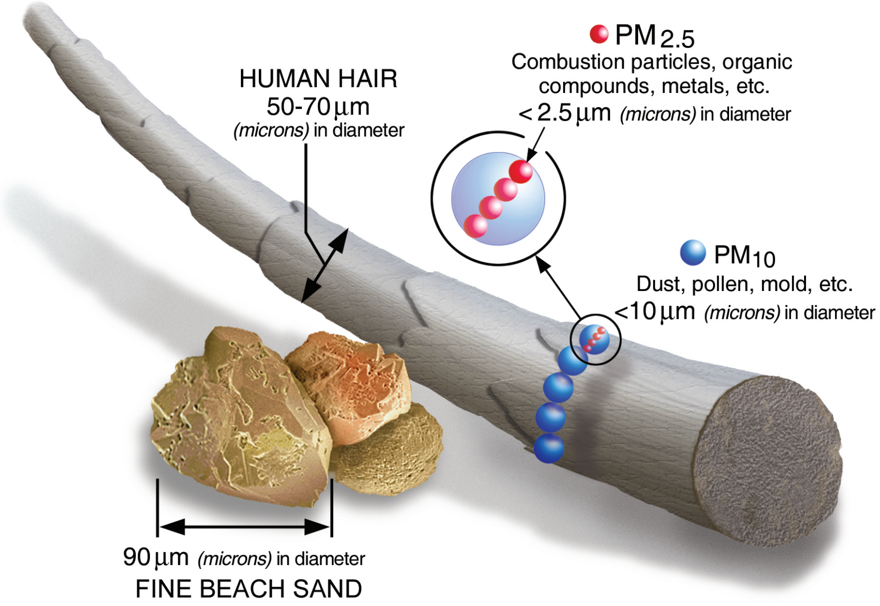

Figure 1.2: Size comparison of PM_{10} and $PM_{2.5}$.

Country	PM fraction	Standards ($\mu g/m^3$)	Averaging time
WHO	PM_{10}	20	Annual
		50	24h
	$PM_{2.5}$	10	Annual
		25	24h
EU	PM_{10}	40	Annual
		50	24h
	$PM_{2.5}$	20	Annual
USA	PM_{10}	150	24h
	$PM_{2.5}$	12	Annual
		35	24h
Australia	PM10	50	24h
	$PM_{2.5}$	8	Annual
		25	24h
Mexico	PM_{10}	75	Annual
		40	24h
	$PM_{2.5}$	45	Annual
		12	24h
Japan	PM_{10}	200	Annual
		100	24h
	$PM_{2.5}$	35	Annual
		15	24h
India	PM_{10}	100	Annual
		60	24h
	$PM_{2.5}$	60	Annual
		40	24h

Table 1.1: PM_{10} and $PM_{2.5}$ regulation in several countries and WHO recommendations, averaged daily (peak) and annually, reprinted from [15].

This method, although very efficient, remains pervasive. Most of the PM monitoring stations are bulky and very expensive. Only a few can be deployed in a small range. In addition to the cost, having only a few sensors to cover a wide area means a coarse monitoring mapping. It does not allow the identification of the exact origin of a PM emission source with high accuracy that would be possible with a very large number of spatially distributed sensors. In order to assess this problem, a attempt using MEMS technologies is made. Thin film bulk acoustic resonators (TFBAR) [16] and quartz-crystal micro balance (QCM) [17] are two interesting candidates: They have two very efficient transducing properties to convert the mass concentration into an electric signal. However, these two systems do not allow size counting, that is to say size distribution over the total PM concentration. Another potential technology, relying on capacitive sensing, will be presented in the next section.

1.3 Interdigital capacitor for PM sensing

The working principle of a capacitive sensor is to convert a capacitance, or a change of capacitance, into an electrical signal. Applied to PM sensing, the capacitance generated by the transducing structure must change in presence of particles. A common architecture is the planar interdigital capacitor (IDC). Two metallic combs are interdigitated and create a fringing electric field. This is a very promising technology thanks to the MOS compatibility fabrication process (CMOS Monolithic transducer). An on-chip sensor based on this technology has been made by Cicarrella et al. in 2016 in [18]. This sensor has a capacitive resolution of 65 zF rms and a signal-to-noise ratio of around 18 dB. For instance, the capacitance shift due to a PM of 1 µm on top of a IDC structure of the same spatial resolution is about 700 zF. Thanks to a very efficient read-out circuit, this demonstration paves the way to IDC capacitive PM sensor. Figure 1.3 shows the transducing part a PM capacitive sensor based on differential IDC. The differential operating mode allows to read out only the capacitance difference between the two IDC induced by the presence of particles on one of them. Indeed, while two signals in phase opposition are applied on the two inputs, there is no charge flow in the charge pre-amplifier if the capacitance of the two IDC are identical. Thanks to a IDC mismatch compensation network, the initial capacitance difference between the two structure (due to process deviation)

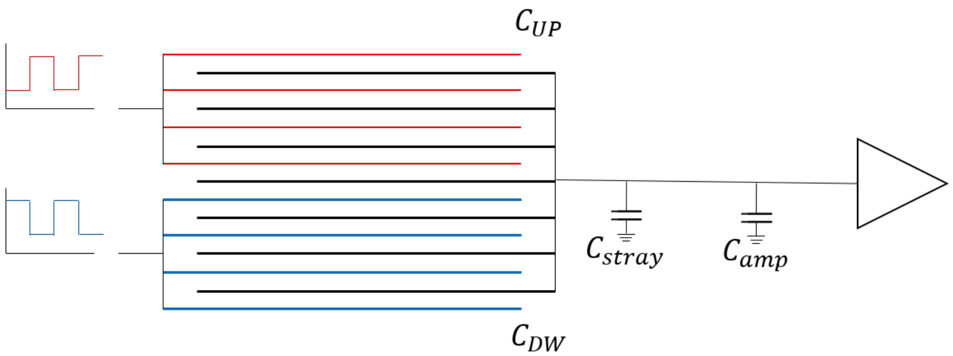

Figure 1.3: Schematic of a differential IDC transducing architecture made of two sets of equal interdigitated electrodes driven by opposite phase signals and sharing the common electrode connected to a charge preamplifier.

is corrected. It lets only the few extra charges generated from the PM polarization to flow out the differential pair.

PM capacitive sensing based on differential IDC has shown promising results and feasibility. However, no proof of concept has been performed yet. Some constraints remain important. For instance, the chemical composition of a particle has an important effect on the capacitance via its relative permittivity. While this parameter is ignored by laser scattering methods, it becomes an issue for complex mixtures capacitive sensing, especially with metallic nano or micro particles. Moreover, the cleaning process after each measurement has to be developed. A burn-off process can be used to remove all the particles on the coating layer, but is efficient at high temperatures only, which can damage the metallic IDC structure.

Fig. 1.4 shows the capacitive change of an IDC in presence of a PM, with respect to its diameter. One can notice the 700 zF difference for a 1 µm diameter with a 1 µm finger width and 50% metalization ratio (this parameter will be defined in the next chapter).

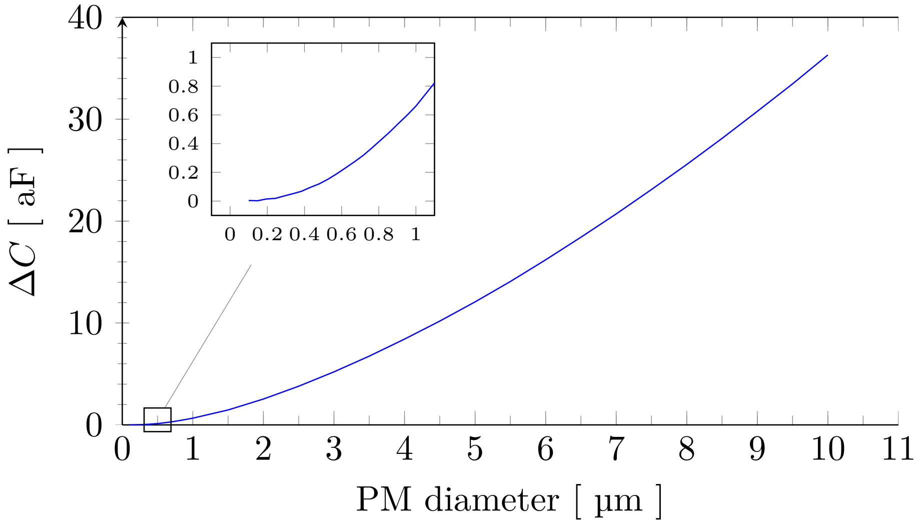

Figure 1.4: Capacitance difference ΔC from FEM 3D simulation with respect to PM diameter for $W = 1\,\mu m$, $\eta = 0.5$, $\varepsilon_{PM} = 2$ and flat electrodes.

2 IDC Capacitance Analytical Model

In this chapter, the physics of fringe capacitance and analytical solutions for field distribution will be explored. In a first part, the concept of conformal mapping will be explained, namely the Schwarz-Christoffel transformation. In a second part, an analytical model for interdigitated electrodes will be presented.

2.1 Conformal Mapping

In order to evaluate the capacitance that a device creates, several solutions can be enforce. One can derive an analytical expression or use computational methods such as Finite Element Method (FEM), for which the result quality is related to the finesse and details of the model. Not to mention that the computational efficiency is closely related to the model simplifications that are made. Among analytical solutions, closed-form expressions for electric field distribution give an exact solution for a given geometry that are therefore very accurate solutions and by definition easy to calculate. Conformal mapping is a strong mathematical tool for field distribution analysis. The efficiency of CM for IDC structure capacitance calculation lies in the nature of the fringe electric field. Such technique enables to express this electric field distribution in a closed-form manner, that is to say through an analytical description.

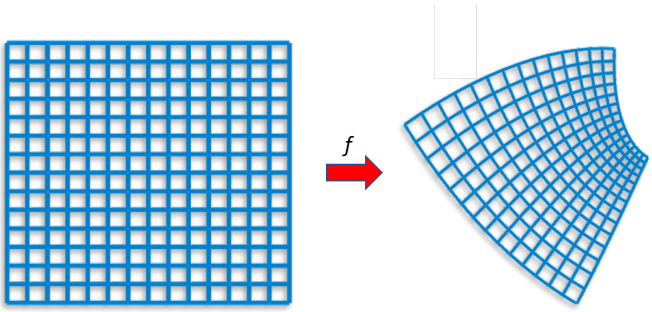

Figure 2.1: Example of conformal mapping process

2.1.1 Basics of conformal mapping

A function f of a complex variable z in the complex domain Z, i.e. $w = f(z)$ with w the value of f at z, can be considered as a mapping function [19]. A mapping (i.e. a complex function) is considered conformal if it preserves angles. Such function sends any point from the original domain Z into a new location on the mapped space. Only a 2-dimentsional mapping (the complex plane Z) will be described, but higher dimensions mapping is feasible, even though the amount of available mapping function is much restricted. Fig. 2.1 is an basic exemple of a grid mapped with a conformal function f.

2.1.2 Schwarz-Christoffel transformation

Schwarz-Christoffel transformation (SCT) is a particular conformal mapping that consists on mapping the x axis from the Z plane into a polygon (simple and closed) in the W plane. Let f be the conformal function that maps the x axis onto a closed polygon of n sides and for which the images through f of these n points x_1, x_2, ..., x_{n-1} and $x = \infty$ are the vertices of that polygon. To obtain the mapping process depicted on Fig.2.2, f is chosen such that

$$f^{'}(z) = A(z - x_1)^{-k_1}(z - x_2)^{-k_2} \cdots (z - x_{n-1})^{-k_{n-1}} \tag{2.1}$$

where A is a constant (that allows some tunability for the polygon size, for instance) and the k_j are real constants. These constants, multiplied by π, represent the argument step of $f^{'}(z)$ when z passes from the left of x_j to the right.

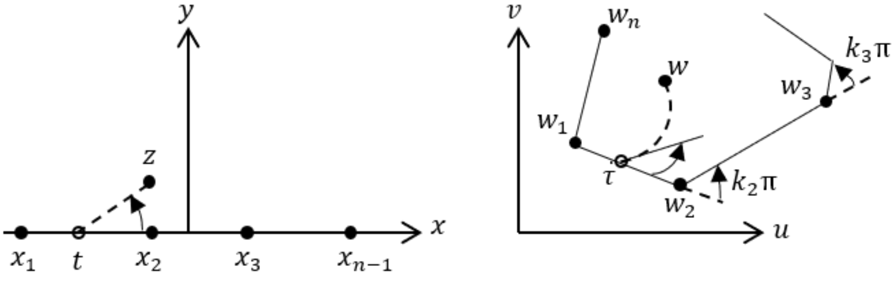

Figure 2.2: Schwarz-Christoffel transformation process of n-1 points (and $x = \infty$) from the x axis with the function f from expression (2.1)

From conformality we can consider $f^{'}(z)$ analytic everywhere in the upper plane except at the n-1 x_j points (demonstrated in [19]). In that case, we can write

$$f(z) = A\int_{z_0}^{z} f^{'}(s)ds + B \tag{2.2}$$

where z_0 is a point in the upper plane where $f^{'}(z)$ is analytic. The Schwarz-Christoffel transformation is defined as the following expression

$$w = A\int_{z_0}^{z}(s - x_1)^{-k_1}(s - x_2)^{-k_2} \cdots (s - x_{n-1})^{-k_{n-1}}ds + B \tag{2.3}$$

2.2 Conformal mapping applied to IDC structure

In this section, conformal mapping method applied to multi-layered interdigital structure will be presented. The first CM model for the study of IDC sensor has been proposed in 1977 by Wei [20]. However this model only considers infinite air layer and is not suitable for a multi-layered structure that would take into account substrate, oxide and sensitive layers that are most of the time part of an IDC sensor structure. In 1994, Wu et al. [21] proposed a first model for multi-layered structure, but poorly accurate. It is in 1996 that Gevorgian et al. [22] proposed a more accurate model still based on CM, but with a different choice for capacitance sub-division. Igreja et al. presented another promising model in 2004 [23] (with an extension in 2011 [24]). These 2 models have been compared experimentally by Feng et al. in 2009 [25]. The results show that Igreja model slightly overestimates the IDC capacitance while Gevorgians's one underestimates it, even though the fingers ending capacitance is neglected in the former one. Igreja model will be presented and adapted for this work, namely because of the extension from 2011 that allows capacitance calculation for both monotonically increasing and decreasing layer's permittivity.

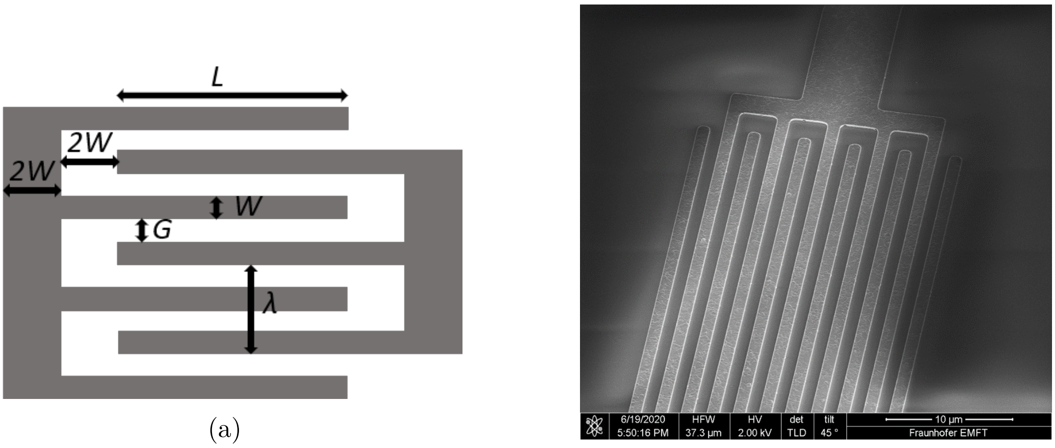

(a)

(b)

Figure 2.3: IDC structure schematic (a) and scanning electron microscopy (SEM) picture of IDC (b).

2.2.1 IDC physical parameters and capacitive model

The physical structure of the IDC is depicted on Fig. 2.3. Fig. 2.3a shows the parameters of a IDC design. W is the width of a finger and G is the gap in between. The finger's ending gap as well as each comb base has been chosen to be equal to twice the finger width. The effective interdigital length, L, represents the length along with the generated electric field is perpendicular to the fingers. The spatial wave length of the IDC is λ, defined as $\lambda = 2(W + G)$. The metalization ratio η represents the fraction of the IDC spatial wavelength that is occupied by metal and is defined as $\eta = W/(W+G)$.

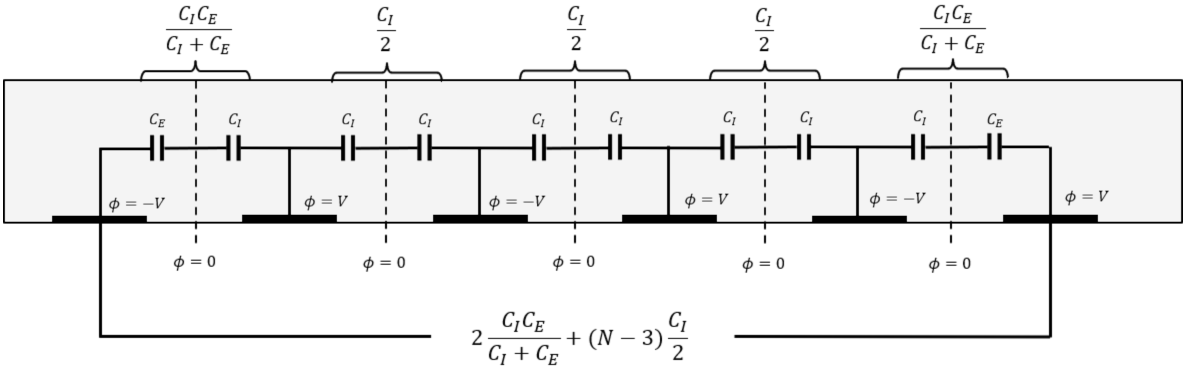

Figure 2.4: IDC cross section equivalent capacitive circuit [23]

The first step of the model consists on decomposing the IDC perpendicular cross-section into sub-divisions for which a capacitance can be attributed. The chosen decomposition is depicted on Fig.2.4, for which the finger's are idealy flat. Because of symmetry, the vertical line at half distance from an electrode to another is an electric wall of equi-potential that has for value the average potential from the surrounding electrodes. In this case, this electric wall is of potential $\phi = 0$. It is a Dirichlet boundary (DB) condition. The electrodes themselves with a potential V or $-V$ satisfy also a DB condition. The total capacitance of the IDC structure from this decomposition is calculated as follow:

$$C = 2\frac{C_I C_E}{C_I + C_E} + (N-3)\frac{C_I}{2} \tag{2.4}$$

2.2.2 Partial Capacitance method

As depicted in Fig. 2.5, a possible way to calculate the multi-layer capacitance is to consider each layer's capacitance contribution. This method is known as the partial capacitance (PC) and has been introduced first in 1995 by Zhu et al. [26]. It has been then demonstrated and adapted for the case of coplanar waveguides (CPW) by Ghione et al. [27]. For a multi-layer configuration for which the permittivity decreases monotonically, the electric field lines at the interfaces tend to be parallel to them. The boundaries can then be attributed a Neumann boundary condition (the derivative of the potential with respect to the normal vector of the boundary is zero, which is in that case perpendicular with the electric field, *i.e.* $\partial\phi/\partial n = 0$). In that case ($\varepsilon_1 > \varepsilon_2 > \cdots > \varepsilon_n$ in Fig. 2.5), the PC method states that the total capacitance is equal to the each layer's capacitance contribution in parallel (PPC). It can be express as:

$$C_I = \sum_{i=1}^{n-1} (\varepsilon_i - \varepsilon_{i+1}) C_{IP}(h_i) + \varepsilon_n C_I(\infty) \tag{2.5}$$

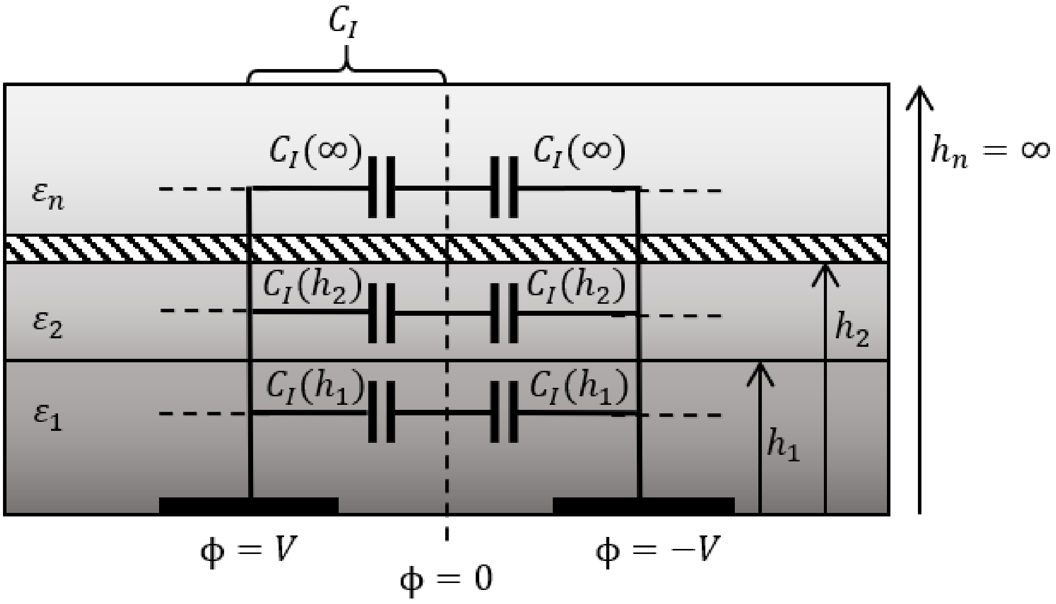

Figure 2.5: Multiple dielectric layers on top of 2 planar and parallel stripes. The partial capacitance method describes the contribution to the total capacitance from each layer.

However, in case the permittivity increases monotonically ($\varepsilon_1 < \varepsilon_2 < \cdots < \varepsilon_n$), the electric field lines at an interface are rather perpendicular to it. It corresponds then to a DB condition. This case has been adapted for IDC by Igreja et al. in the extension of his model [24]. The capacitance contribution for each layer is then considered as in series (SPC), expressed by the following formula:

$$\frac{1}{C_I} = \sum_{i=1}^{n-1} (\frac{1}{\varepsilon_i} - \frac{1}{\varepsilon_{i+1}}) \frac{1}{C_{IS}(h_i)} + \frac{1}{\varepsilon_n C_I(\infty)} \tag{2.6}$$

2.2.3 CM model for C_I and C_E

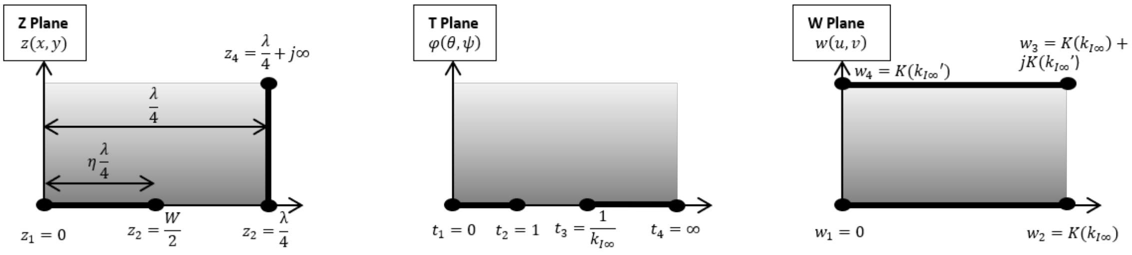

Figure 2.6: CM process for $C_I(\infty)$ from the Z plane to the W plane. The planar electrode and the vertical electric wall are mapped into a plate-to-plate capacitance configuration.

Each physical configuration (PPC and SPC, C_I and C_E, infinite and finite layer) is different and thus requires a different mapping. In this section, the conformal mapping approach from [23] for C_I and an infinite top air layer will be detailed. This particular case will be developed further in chapter 3 for the case with a particle.

The process consists on mapping the Z plane into the W plane, via an intermediate transformation. As depicted on the schematics from Fig. 2.5, the Z plane corresponds, for the $C_I(\infty)$ case, to 2 DB and 3 NB conditions: (DB i) half an electrode; (DB ii) the vertical electric wall in between two electrodes; (NB i) the vertical line that cuts in half an electrode; (NB ii) the upper boundary (infinitely high in that case); (NB iii) the space between the electrode and the electric wall.

The transformation from the Z plane to the intermediate T plane is operated through the function:

$$T(z) = \frac{1}{k_{I\infty}} \sin(\frac{2\pi}{\lambda} z) \tag{2.7}$$

with $k_{I\infty} = sin(\frac{\pi}{2}\eta)$. The T plane is then mapped into the W one by the use of the Schwarz-Christoffel transformation. The upper-right quadrant of the T plane is into a rectangle delimited by the 4 points t_1, t_2, t_3 and t_4. Such transformation, with $k_1 = k_2 = k_3 = k_4 = -1/2$ for a rectangle 2.6, is expressed into the SCT as following:

$$W(t) = \int_0^t \frac{dt'}{\sqrt{(t'-t_1)(t'-t_2)(t'-t_3)}} = \int_0^t \frac{dt'}{\sqrt{t'(t'-1)(t'-\frac{1}{k_{I\infty}})}} \tag{2.8}$$

This integral can be rewritten [19]:

$$W(t) = F(\varphi,k_{I\infty}) = \int_0^{\varphi} \frac{dw'}{\sqrt{(1-w'^2)(1-k_{I\infty}^2 w'^2)}} \tag{2.9}$$

with F the elliptic integral of first kind with modulus $k_{I\infty}$ and amplitude φ such that $sin(\varphi) = sn(W(t)) = T(z)$, with sn is the Jacobi elliptic function [28].

The four points t_1, t_2, t_3 and t_4 are actually chosen so that the amplitude φ is $\pi/2$ (or 0) at those points. The four points are mapped into the W plane as $w_1 = 0$, $w_2 = K(k_{I\infty})$, $w_3 = K(k_{I\infty}) + jK(k'_{I\infty})$ and $w_4 = jK(k'_{I\infty})$ ([28], table 16.5). In this new configuration, the two electrodes (thick lines on Fig. 2.5) are into a plate-to-plate capacitor geometry. The electric field fringe lines are transformed into straight lines, that is to say into a uniform electric field along the y axis. The capacitance $C_I(\infty)$ can be derived easily:

$$C_I(\infty) = \varepsilon_0 \varepsilon_r L \frac{K(k_{I\infty})}{K(k_{I\infty'})} \tag{2.10}$$

with ε_0 the vacuum permittivity, ε_r the relative permittivity of the layer's media and L the effective length of the IDC.

For generalisation, the physical configurations for PPC and SPC cases are showed on Fig. 2.7, including interior and exterior capacitance. The corresponding CM transformation are exhibited in table 2.1. For the case of infinite layer ($h = \infty$), the transformation functions for C_I and C_E are simplified ($C_I(\infty)$ has been derived previously in expression 2.10). In this case of infinite height, the SPC approach does not differ from the PPC one and $C_{IP} = C_{IS}$, $C_{EP} = C_{ES}$.

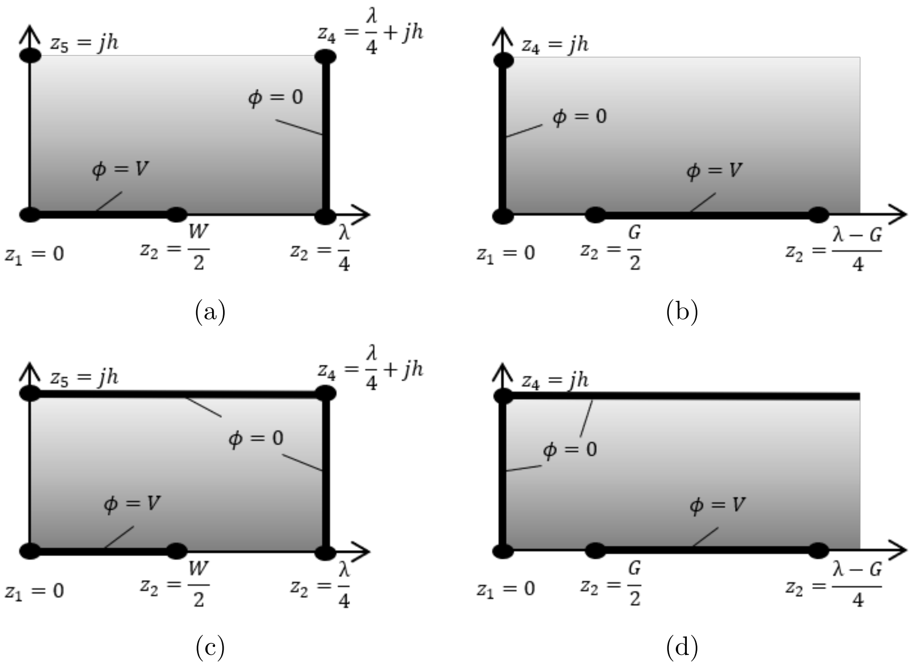

Figure 2.7: Physical configurations (Z plane) for C_I and C_e calculation: C_{IP} (a); C_{EP} (b); C_{IS} (c); C_{ES} (d). The thick lines are DB conditions while the other boundaries of the inner area are NB conditions ($\partial\phi/\partial n = 0$).

	Interior electrodes		Exterior electrodes	
	SPC ($\varepsilon_1 < \varepsilon_2 < \cdots < \varepsilon_n$)	PPC ($\varepsilon_1 < \varepsilon_2 < \cdots < \varepsilon_n$)	SPC ($\varepsilon_1 < \varepsilon_2 < \cdots < \varepsilon_n$)	PPC ($\varepsilon_1 < \varepsilon_2 < \cdots < \varepsilon_n$)
Finite layer	$C_{IS} = \varepsilon_0 L \frac{K(k_{IS}}{K(k'_{IS}}$ $k'_{IS} = \sqrt{1 - k_{IS}^2}$ $k_{IS} = t_2$ $t_2 = sn(K(k)\eta{,}k)$ $t_4 = \frac{1}{k}$ $k = (\frac{\nu_2(0{,}q)}{\nu_3(0{,}q)})^{2*}$ $q = exp(-4\pi r)$	$C_{IP} = \varepsilon_0 L \frac{K(k_{IP}}{K(k'_{IP}}$ $k'_{IP} = \sqrt{1 - k_{IP}^2}$ $k_{IP} = \sqrt{\frac{t_4^2 - 1}{t_4^2 - t_2^2}}$ $t_2 = sn(K(k)\eta{,}k)$ $t_4 = \frac{1}{k}$ $k = (\frac{\nu_2(0{,}q)}{\nu_3(0{,}q)})^2$ $q = exp(-4\pi r)$	$C_{ES} = \varepsilon_0 L \frac{K(k_{ES}}{K(k'_{ES}}$ $k'_{ES} = \sqrt{1 - k_{ES}^2}$ $k_{ES} = \sqrt{\frac{t_4 - t_3}{t_4 -}}$ $t_3 = cosh(\frac{\pi(1-\eta)}{4r})$ $t_4 = cosh(\frac{\pi(1+\eta)}{4r})$	$C_{EP} = \varepsilon_0 L \frac{K(k_{EP}}{K(k'_{EP}}$ $k'_{EP} = \sqrt{1 - k_{EP}^2}$ $k_{EP} = \frac{1}{t_3}\sqrt{\frac{t_4^2 - t_3^2}{t_4^2 - 1}}$ $t_3 = cosh(\frac{\pi(1-\eta)}{8r})$ $t_4 = cosh(\frac{\pi(1+\eta)}{8r})$
Infinite layer	$C_I(\infty) = \varepsilon_0 L \frac{K(k_{I\infty}}{K(k'_{I\infty}}$ $k_{I\infty} = \sin(\frac{\pi}{2}\eta)$		$C_E(\infty) = \varepsilon_0 L \frac{K(k_{I\infty}}{K(k'_{I\infty}}$ $k_{I\infty} = \frac{2\sqrt{\eta}}{1+\eta}$	

Table 2.1: Transformation process equations for PPC and SPC cases reprinted from [24]. $^*Thetafunctions$ [28]

2.2.4 Capacitance from electrode thickness

So far, the electrodes have been considered as idealy flat. However for any kind of IDC structure, the electrodes have a well defined thickness that create a transversal electric field in the gap, in between two vertical walls of the fingers. This component should often not be neglected for IDC structure when the thickness of the fingers is too important. In order to include this parameter in the capacitance calculation process, Wheeler proposed in 1965 [29] a method to take the thickness of the electrode into account. It consists on considering the thick electrodes as flat but with an incremented effective width, described in the following expresions:

$$\Delta W = \begin{cases} \frac{t}{\pi}(1+ln(\frac{4\pi W}{t})), & \text{if} \frac{W}{h} \leq \frac{1}{2\pi} \\ \frac{t}{\pi}(1+ln(\frac{h}{t})), & \text{otherwise} \end{cases} \tag{2.11}$$

with ΔW the width increment to W, t the thickness of the fingers and h the thickness of the dielectric layer in which the electrodes are. However, this model seems not to be efficient for consequent metal thickness. A potential alternative for non negligible thickness is to consider a transversal and uniform field in between the walls of two electrodes. It means to consider a plate-to-plate type capacitance C_{trans} that can be calculated as follow:

$$C_{trans} = \frac{\varepsilon_0 \varepsilon_r L t \eta}{(W(1-\eta))} \tag{2.12}$$

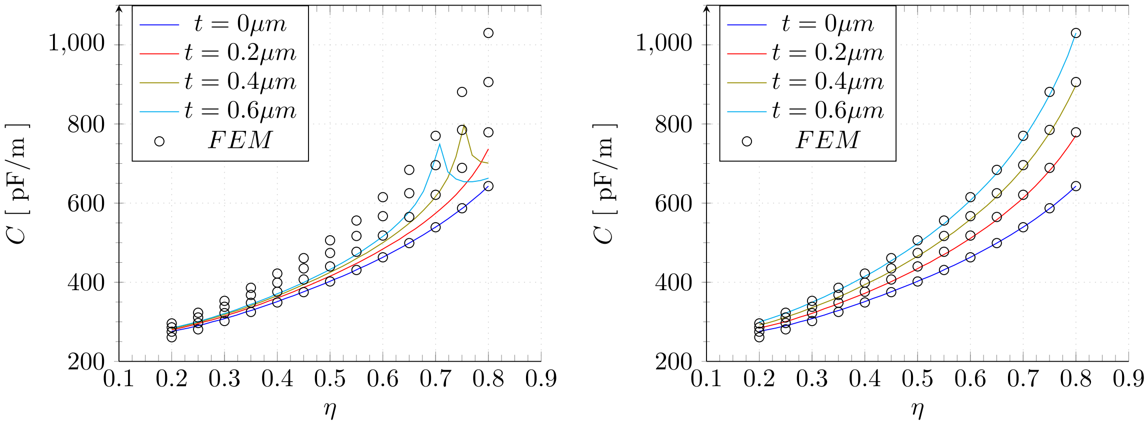

(a) (b)

Figure 2.8: IDC model capacitance per unit of length value comparison with FEM. The capacitance is calculated with respect to η for different fingers thickness. FEM *versus* Wheeler effective width model [29] (a), FEM *vs* transversal field component model (b). The IDC design parameters refer to the design from Chapter 4 with $N = 19$, $W = 1\,\mu\text{m}$, $\varepsilon_{SiO_2} = 3.9$, $\varepsilon_{Si} = 11.7$ and $h_{SiO_2} = 2\,\mu\text{m}$.

with ε_r the relative permittivity of the medium. The gap G in between two electrodes being equal to $W(1-\eta)/\eta$. These two models are compared with FEM simulation on Fig 2.8.

2.2.5 Capacitance from fingers ending

The fingers ending capacitance is often neglected but can have a significant impact if the effective interdigitated length L is not very large compared to the spatial wavelength of the IDC times the number of fingers. Gevorgian et al. proposed an evaluation of this capacitance [22] using conformal mapping. The design will be considered as that of Fig. 2.3 since these are the parameters of the experimental structures that will be detailed in chapter 4. The gap between the end of the finger and the perpendicular comb pad is then twice the finger width, as well as the comb pad itself. The model for the finger ending capacitance is depicted on Fig. 2.9. As shown in [22], the value of the ending capacitance converges toward a good approximation for $x > W/2$. One can then set the magnetic wall at $x = 2W$. In that case, the configuration is such that one can consider the finger ending capacitance as two external capacitances C_E in series. The possible configurations are depicted on Fig 2.7 (b) and (d), for finite or infinite layer. The multi-layer process can be applied and C_E is evaluated for $\eta = 0.5$ and the total end capacitance for one finger is $C_E/2$. For thick electrodes, the transversal field for one finger's end can also be evaluated as $C_{trans} = \varepsilon t/2$.

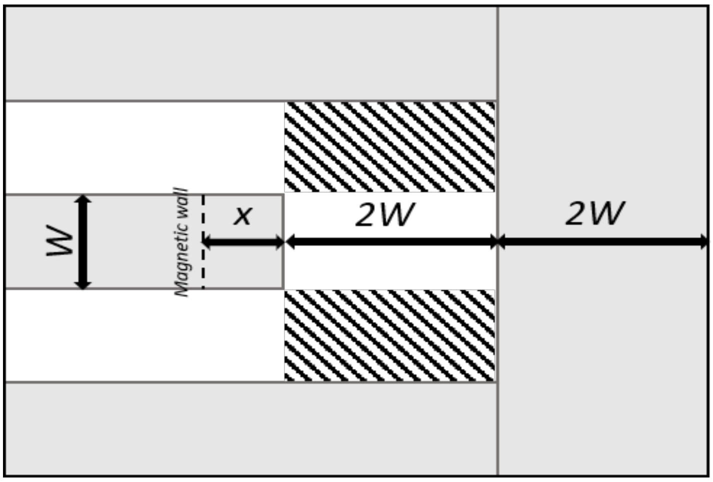

Figure 2.9: Model for fingers ending capacitance from [22]. The dashed region are not evaluated because too complex.

3 PM Capacitance Analytical Model

Analytical models derived from conformal mapping have already proven to be very efficient and accurate for simple design but also for multi-layered dielectric structure (PPC and SPC cases). For a differential IDC pair for PM sensing, each IDC capacitance value has a great impact on the noise to the charge preamplifier stage [18]. This noise mostly defines the limit of detection of the sensor, a particle being detected if the output generated charge is significantly higher than the noise. Beside, for a perfectly balanced differential pair, the charge flow at the output is only induced by the increment of capacitance when a particle lands on top of the interdigital structure. It is then important to quantify the capacitive effect of a particle to the IDC. Due to the PM permittivity (higher than air), the electric field density is enhanced where the particle lands and around. Since the field on top of the electrode is not uniform along one direction, it is complicated to analyse it once the presence of a PM. In this chapter, an analytical model is developed to calculate the capacitance induced by a PM on top of an IDC.

3.1 Spherical PM through conformal mapping

Assuming the PM to have an evenly distributed geometry, the most general way to simulate it is to consider it as a sphere. FEM simulation remains so far the only viable computational method for PM capacitive simulation. If the size of the particle is about the same range or bigger than the spatial wavelength of the IDC, FEM simulation can give a relatively good result. The finesse of the meshing process also improve the result quality but in exchange of a consequent computational time. An important cons for FEM is that the capacitance difference must be calculated in 3 dimensions and becomes then a much more complicated simulation. Indeed, if one considers the IDC cross-section containing the PM cut in the middle, there is no way to retrieve the total capacitance difference for the 3D model. In order to develop a closed-form expression for the capacitive shift induced by a PM, one can try to include the particle through the conformal mapping process. Whatever the geometry of the entity that emerges, it is guaranteed by superposition that this mapped PM would be put in the uniform electric field in the W plane.

Since a particle that lands on top of the IDC only disturbs the electric field in the air layer, it is sufficient to map the infinite air layer only, with the PM, in order to calculate ΔC. The fingers will be assumed flat. It means that ΔC becomes less dependent on the landing position. It also guarantees that the calculated capacitance value is a lower bound for a certain diameter.

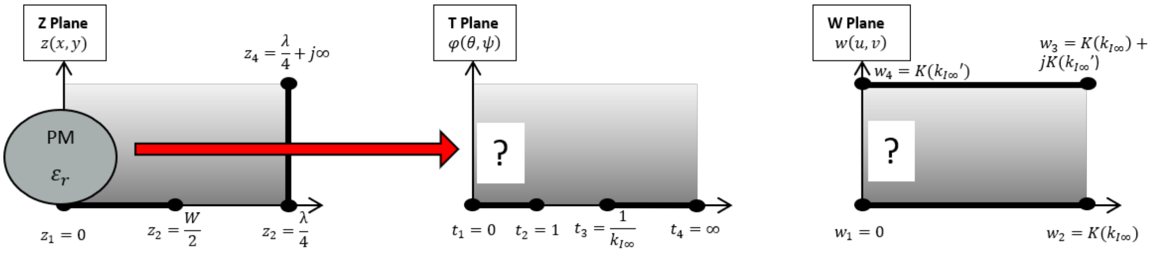

Figure 3.1: Conformal mapping process attempt of C_I cell including half a PM that lands in the middle of a finger.

A first limitation to this method is the size of the PM one can map. Indeed, the radius of the particle in the middle of an electrode must fit in the C_I sub-division, that is to say $d_{max} = \lambda/4$ (Fig. 3.1). Except this, the case that will be assumed is a PM in the middle of an electrode. The new Z plane for C_I now contains a half disc of radius that of the PM. The CM process that has been detailed in section 2.2.3 will be developed in order to map any point of the Z plane into the W plane. It will allow to discretize the half disc and send its peripherical points into the W plane. The mapping functions $T(z)$ and $W(t)$ remain obviously the same and the method can be extended to any complex point z:

$$\sin(\varphi) = T(z) = \frac{1}{k_{I\infty}} \sin(\frac{2\pi}{\lambda} z) \tag{3.1}$$

$$\varphi = \arcsin(\frac{1}{k_{I\infty}} \sin(\frac{2\pi}{\lambda} z)) \tag{3.2}$$

with φ a complex number such that $\varphi = \theta + j\psi$ and θ and ψ are real numbers. The corresponding point in the W plane is given by equation 2.9:

$$w = F(\varphi,k_{I\infty}) \tag{3.3}$$

The incomplete integral of first kind cannot be solved directly with a complex amplitude, however a change of variable is possible [28]:

$$F(\varphi,k_{I\infty}) = F(\alpha,k_{I\infty}) + jF(\beta,k'_{I\infty}) \tag{3.4}$$

with α and β such that $1/tan^2(\alpha)$ is the positive root of

$$x^2 - \left[\frac{1}{\tan^2(\theta)} + k_{I\infty}^2 \frac{\sinh^2(\psi)}{\sin^2(\theta)}\right] x - k'^2_{I\infty} \frac{1}{\tan^2(\theta)} = 0 \tag{3.5}$$

and β is derived from α as following:

$$k_{I\infty}^2 \tan^2(\beta) = \frac{\tan^2(\theta)}{\tan^2(\alpha)} - 1 \tag{3.6}$$

Combining equations from 3.2 to 3.6 allows to send any point from the Z plane to the W plane. A spherical PM can be represented in 2 dimensions by a disc, and can be discretized with points on its edge. With a sufficient number of points that are mapped, it is possible to build the new mapped geometry of the half disc. The FIg. 3.2 shows the result of the mapping of a few half discs. An important remark that is to be made is that, above a diameter of the size of the electrode, W, (or a radius of $W/2$), the shape of the mapped half disc does not seem to be a common geometrical entity (see the deformed ellipses on Fig. 3.2b). However, for any disc that is mapped in the middle of an electrode, for which the diameter does not exceed it, one can state that the mapped geometrical object is close to an ellipse (or a semi ellipse if one considers one mapped area at a time). No rigorous mathematical demonstration has been made in this work. A possible approach is to prove that for any point $z = x + jy$ on the disc in the Z plane, that is solution of the circle identity:

$$\frac{x^2 + y^2}{r^2} = 1 \tag{3.7}$$

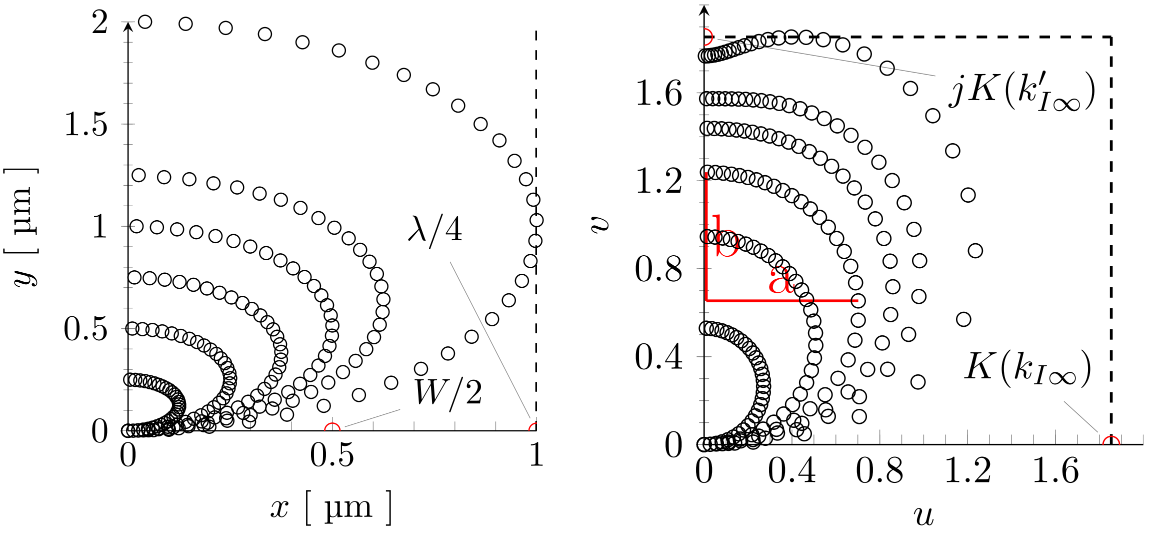

(a)

(b)

Figure 3.2: Example of CM process with half PM placed in C_I subsection representing the Z plane (a) and the W plane (b). The PM diameter varies from 0.25 µm to 2 µm, the width of the section $\lambda/4$.

is, once transformed, solution of an ellipse identity. That is to say the corresponding point $w = u + jv$ is solution of

$$\frac{u^2}{a^2} + \frac{v^2}{b^2} = 1 \tag{3.8}$$

with a and b the parameters of the ellipse.

Instead, any supposedly ellipse has been compared with a real ellipse of same parameters a and b, numerically computed as follow:

- a is the highest x axis component among the computed points.
- b is calculated as $(W(z_0) - W(z_1))/2$ with z_0 and z_1 such that $arg(z_0) = arg(z_1) = \pi$ (that is to say the two points at the bottom and the top of the vertical axis).

Not to mention that it can also be mapped with a certain elevation, leading to a smaller ellipse with different parameters. Since the PM is supposed to have landed on the IDC, only 0 elevation PM will be considered. In order to computationally determine the shape matching with the mapped geometrical shape, a possible protocol is to calculate the absolute relative error for any point of the shape with respect to the points with same phase of the real ellipse made of the parameters a and b. In other word, for a mapped point w of phase θ, the error at this point is calculated as follow:

$$error = \frac{||w - \nu||}{||\nu||} \tag{3.9}$$

with $\nu = a \times cos(\theta) + b \times sin(\theta)$, a and b being determined as previously explained.

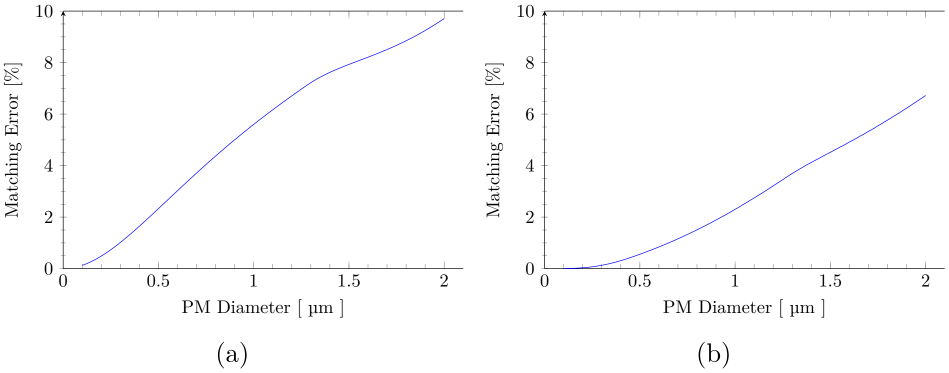

Figure 3.3: Matching Error with a real ellipse. (a) is the error calculated from formula 3.9. (b) shows the error from the vertical method.

The Fig. 3.3 shows the matching error with the mapped shape and a real ellipse whose parameter are determined arbitrarily as explained above. As expected, the ellipse approximation is more accurate for very small PM. However, one could expect an abrupt increase of the matching error for diameters above W but it is not the case for this matching method. Another matching evaluation can be performed by comparing the point to point vertical difference between the mapped shape and the corresponding real ellipse. In that case, the matching error is lower, namely for very small PM. No other rigorous and efficient matching evaluation has been found.

According to Fig. 3.2a, and because the PM is supposed in the middle of an electrode, it will affect two C_I cells at a time. The symmetry between those two cells being perfectly kept even with the PM, the two capacitances are still considered in parallel. It means that if one considers only one C_I cell and the half disc, the capacitance increment $\delta C = (C - C_i)/C_i$ induced by the PM will lead to a cell capacitance $C_I(1 + \delta C)$. In order to calculate the capacitance increment from the entire PM, one has to consider the entire disc, and so two C_I cells, then the initial capacitance would be $2C_I$ and the increment is $2\delta C$. The change is capacitance is then doubled.

3.2 Ellipsoid in uniform electric field

The study of effective permittivity of a media in which is diluted dielectric ellipsoids has been performed in 2002 by Giordano S. [30]. This study has been used to demonstrate the effect of dielectric admixtures, modeled as ellipsoids, to the capacitance of a plane capacitor in 2007 by Vibralis J.A. [31].

First of all, as mentioned in subsection 3.1, there is no simple way to retrieve the total capacitance including the PM from the 2 dimension cross section. However, one can consider the 3D ellipsoid of parameter a, b and extrude the W plane along the z axis from the Z plane. This hybrid space will be called W_z. Without the PM, it is equivalent to multiply the cross-section capacitance C_I by the IDC length L (what has been done in expression 2.10). With the PM, one can assume that the ellipse is an ellipsoid of third parameter c being equal to the PM radius. The problem has now been transformed into a dielectric ellipsoid of parameters a, b, and c, in an uniform electric field in between two parallel plates of surface area $S = L \times K(k_{I\infty})$ and distant from $K(k'_{I\infty})$.

For simplicity, one can suppose the base (q,r,s) of the ellipsoid to coincide with the base (u,v,z) of the space W_z. This is the case since the ellipsoid is already oriented along (u,v,z) with respect to its parameters. The initial electric field density $\boldsymbol{D_0}$ (EFD) is related to the electric field, when uniform, as following:

$$\boldsymbol{D_0} = \varepsilon_0 \varepsilon_{air} \boldsymbol{E_0} \tag{3.10}$$

with ε_0 the vacuum permittivity and ε_{air} the relative permittivity of air, supposed isotropic. In this case, the electric field is uniform along the v axis, perpendicular to the plates. The EFD inside the particle $\boldsymbol{D_p}$ is also uniform along v [14], and expressed as following:

$$\boldsymbol{D_p} = \begin{bmatrix} 0 & D_{pv} & 0 \end{bmatrix}^T = \boldsymbol{A} \cdot \begin{bmatrix} 0 & D_{0v} & 0 \end{bmatrix}^T \tag{3.11}$$

with $\boldsymbol{A} = \begin{bmatrix} A_a & 0 & 0 \\ 0 & A_b & 0 \\ 0 & 0 & A_c \end{bmatrix}$ and $D_{0v} = \varepsilon_0 \varepsilon_{air} E_{0v}$. The coefficients A_i, for $i = a{,}b{,}c$ are the shape coefficients of the ellipsoid:

$$A_i = \frac{\varepsilon_p/\varepsilon_{air}}{1 + L_i\left[(\varepsilon_p/\varepsilon_{air}) - 1\right]} \tag{3.12}$$

with ε_p the relative permittivity of the PM. and L_i the depolarization factor [30]:

$$L_i = \frac{abc}{2} \int_0^\infty \frac{dt}{R(t)(t + i^2)} \tag{3.13}$$

with $R(t) = \sqrt{(t + a^2)(t + b^2)(t + c^2)}$. The total EFD including the PM is evaluated as following:

$$\boldsymbol{D} = k\boldsymbol{D_p} + (1 - k)\boldsymbol{D_{air}} \tag{3.14}$$

with $\boldsymbol{D_p}$ defined previously as the EFD inside the PM, $\boldsymbol{D_{air}}$ the EFD outside the PM and k the volume ratio of the half ellipsoid with respect to the total volume of the extruded C_I cell:

$$k = \frac{\frac{2}{3}\pi abc}{K(k_{I\infty})K(k'_{I\infty})L} \tag{3.15}$$

The EFD $\boldsymbol{D_{air}}$ outside the PM is not uniform and then not equal to the initial uniform EFD. Instead, the electric field is distorted around the PM. Fig. 3.4 shows the corresponding electric field lines before and after mapping. The distortion field $\boldsymbol{D'} = \boldsymbol{D_{air}} - \boldsymbol{D_0}$ [31] around the PM is clearly identifiable. In order to evaluate it, $\boldsymbol{D'}$ is expressed in function of $\boldsymbol{D'_\infty}$, the distortion field around a metallic particle, which is the particular case of $\varepsilon_p = \infty$.

On can defined the demagnetizing factor matrix $\boldsymbol{K} = \begin{bmatrix} \kappa_a & 0 & 0 \\ 0 & \kappa_b & 0 \\ 0 & 0 & \kappa_c \end{bmatrix}$ such that for $i = a{,}b{,}c$,

$$\kappa_i = \frac{L_i\left[(\varepsilon_p/\varepsilon_{air}) - 1\right]}{1 + L_i\left[(\varepsilon_p/\varepsilon_{air}) - 1\right]} \tag{3.16}$$

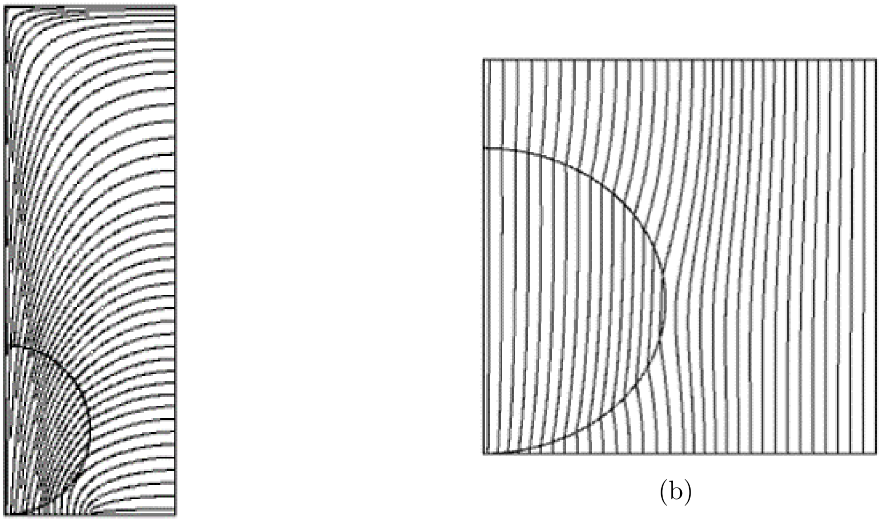

(b)

(a)

Figure 3.4: FEM simulation with the PM from Z plane configuration (a) and W plane configuration (b) (not scaled). Both simulation give the same result.

The demagnetizing factor matrix has been introduced for the first time in 1945 in [32]. $\boldsymbol{D'}$ relates to $\boldsymbol{D'_\infty}$ through:

$$\boldsymbol{D'} = \boldsymbol{K}\boldsymbol{D'_\infty} \tag{3.17}$$

As it has been be shown [31], in average over the orientation of the ellipsoid, $\overline{\boldsymbol{D'_\infty}} = k\boldsymbol{D_0}$. It leads to $\overline{\boldsymbol{D'}} = \kappa_b k D_0$. The relative variation of electric field density is then given by;

$$\delta D = \frac{D_p - D_0}{D_0} k + \frac{\overline{\boldsymbol{D'}}}{D_0}(1-k) = (A_b - 1)k + \kappa_b k(1-k) \tag{3.18}$$

3.3 Ellipsoid capacitance effect

3.18 allows one to calculate the increment of the electric field density due the the PM. Besides, the capacitance created by a parallel plate capacitor of surface S with a distributed charge q with density σ and a potential difference U is given by:

$$C = \frac{q}{U} = \frac{\sigma S}{U} = \frac{DS}{U} \tag{3.19}$$

The capacitance increment due to the PM is then calculated as following:

$$\delta C = \frac{C - C_0}{C_0} = \frac{(S/U)(D - D_0)}{(S/U)D_0} = \frac{D - D_0}{D_0} = \delta D \tag{3.20}$$

The capacitance increment can then be calculated from 3.18. In order to calculate the capacitance difference of the IDC with and without PM, the formula from Fig. 2.4 combined with 3.20 give:

$$\Delta C = (2\frac{\delta C + 1}{\delta C + 2} - 1)C_i \tag{3.21}$$

A first limitation to this model is the validity of L_i. Indeed, 3.13 assumes that the dielectric ellipsoid concentration is highly diluted: In other word, this expression is valid only for small k, which is not the case here. However, the Bruggeman procedure, detailed in [30], developped further the depolarization factor evaluation and extended the domain of validity for any value of k. The new depolarization factors evaluated from the parameters e and g defined as $e = a/c$ and $g = a/c$. These two parameters and the ellipsoid parameters must satisfy the following assumptions:

$$0 < a < b < c \quad ; \quad 0 < e < 1 \quad ; \quad 0 < g < 1 \tag{3.22}$$

The depolarization factors are then given by:

$$L_a = \frac{1}{1-e^2} - \frac{e}{(1-e^2)\sqrt{1-e^2g^2}}E(\nu,q) \tag{3.23}$$

$$L_b = \frac{e(1-e^2g^2)}{(1-e^2)(1-g^2)\sqrt{1-e^2g^2}}E(\nu,q) - \frac{eg^2}{(1-g^2)\sqrt{1-e^2g^2}}F(\nu,q) - \frac{e^2}{1-e^2} \tag{3.24}$$

$$L_c = \frac{eg^2}{(1-g^2)\sqrt{1-e^2g^2}}\left[F(\nu,q) - E(\nu,q)\right] \tag{3.25}$$

with $\nu = \arcsin(\sqrt{1-e^2g^2})$, $q = \sqrt{\frac{1-g^2}{1-e^2g^2}}$ and F, E the elliptic integrals of first and second kind, respectively, defined as:

$$F(\nu,q) = \int_0^{\sin(\nu)} \frac{dx}{\sqrt{(1-x^2)(1-q^2x^2)}} \tag{3.26}$$

$$F(\nu,q) = \int_0^{\sin(\nu)} \frac{\sqrt{1-q^2x^2}}{\sqrt{1-x^2}}dx \tag{3.27}$$

While $0 < a < b$ is not always satisfied in 3.22, c is around a micro meter and is, with e and g, largely out of range. Then, if $0 < c < a < b$, then the two parameters b and c can be switched, $b \leftrightarrow c$. In that case, the axis in the elctric field direction becomes c and the depolarization factor is then calculated with the L_c formula 3.25. In case $0 < c < b < a$, then the parameters a and c are also switched accordingly, $a \leftrightarrow c$. The depolarization factor along the electric field direction remains L_b but calculated for the new parameters that have been permuted.

Another way to proceed would be to multiply c by a sufficiently high number in order to satisfy the inequalities 3.22. Indeed, it can be noticed that in the δC expression, k is invariant to homothetic transformation (multiplying all the paramters a, b, c, L, $K(k_{I\infty})$ and $K(k'_{I\infty})$ by a real number). Only the depolarization factors are sensitive to a multiplication factor. For a and b around 1, δC converges to the same value calculated from the previous paragraph for $h > 10^8$, h being the homothety factor.

Fig. 3.5 plots the ΔC capacitance difference induced by a PM from the model compared with FEM. As it will be summarized in section 3.4, the accuracy of the model decreases when the PM diameter is larger than W, until it reaches $\lambda/2$, being the physical limit of the model.

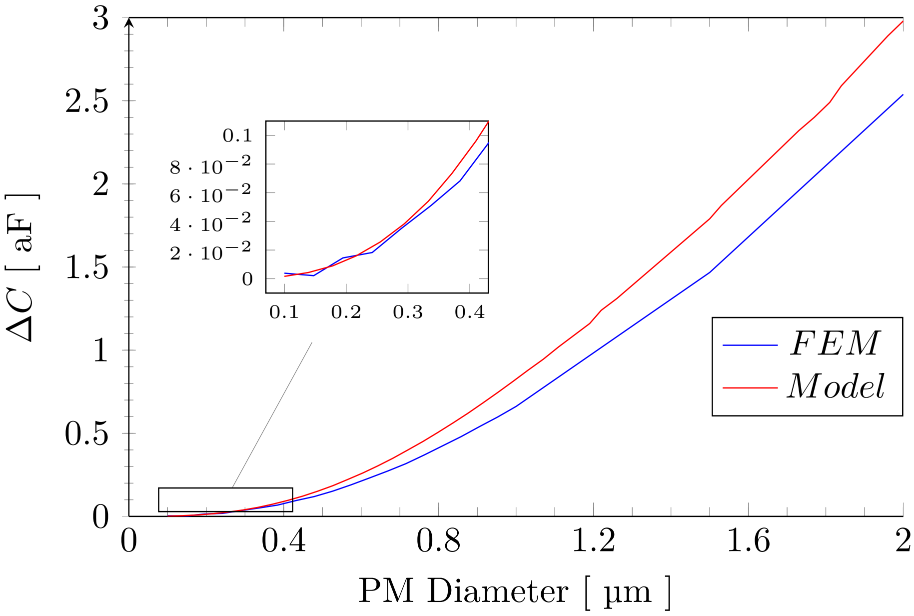

Figure 3.5: ΔC values for different PM diameter. $\varepsilon_p = 2$, $W = 1\,\mu\text{m}$, $\eta = 0.5$, $L = 10\,\mu\text{m}$ (Ł is taken large enough so that it is seen as infinite from the PM, but sufficiently small for the FEM simulation).

3.4 Model limitations

This model has three limitations from three assumptions that have been made:

- The initial NB condition between points z_2 and z_3 in the Z plane or between w_2 and w_3 in the W plane (Fig. 2.5) cannot be considered as such in presence of the PM, especially for important diameter (The vertical electric field line is deformed). It also means that the C_I neighbor cells are affected by the PM and this is not taken into account in the ΔC calculation.

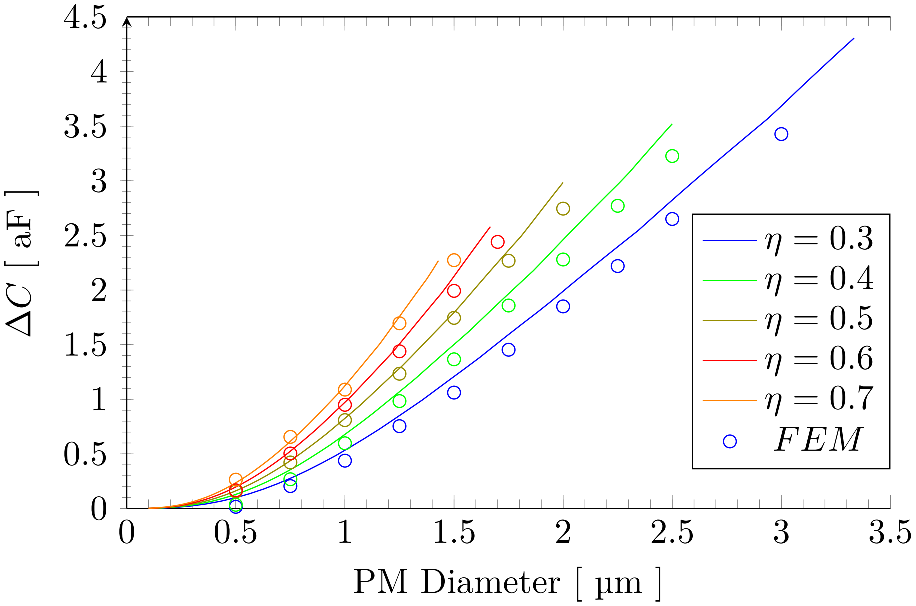

Figure 3.6: ΔC values with respect to PM diameter for different values of η, $W = 1\,\mu\text{m}$, $\eta = 0.5$, $L = 10\,\mu\text{m}$. The diameter range goes from $0.1\mu m$ to $\lambda/2 = W/\eta$ for each different value of η.

- Ellipse shape, for which the matching error to a real ellipse increases with the diameter.
- Ellipsoid shape of the PM in the W_z hybrid space.

These limitations show why the model does not match very well with FEM for PM diameter of the range of $\lambda/2$. However, with very small PM, the model converges toward an exact closed-form analytical expression. In the meantime, FEM accuracy remains very low for small geometrical entities compared to the total volume. In order to determine the range of this model, the ratio $\tau = d/\lambda$ is introduced, with d the PM diameter. It represents the ratio between the PM radius and the C_I cell width. It follows that the model is valid for τ between 0 and 1. For an electrode width $W = 1\,\mu\text{m}$ and $\eta = 0.5$, the capacitance difference for $\tau = 0.5$ ($1\mu m$ diameter PM) has been simulated from 600 zF to 600 zF for a slightly different mesh finesse. It means in this case that the model is more convenient than the FEM simulation. Indeed, for few tenth micro meter diameter (see Fig. 3.5), the result from FEM seems quite inaccurate as the capacitance change for 0.2 µm PM diameter is lower than for 0.1 µm.

4 IDC Structure Characterization

In order to characterize experimentally an IDC, a couple of MOS compatible IDC structures have been made in-house. In this chapter, the specifications of the IDC design will be described. In a second part, the measurement setup and some results will be presented.

4.1 Fabrication process specifications

The physical part of the sensor, the interdigital capacitor transducer, has been produced in quantity for a large panel of parameters for characterisation purpose. The substrate on which the IDC structures have been produced is a 200 mm p-doped (Boron) silicon wafer. The doping concentration is relatively low leading to a resistivity ρ between $1\,\Omega\,\mathrm{cm}$ and $50\,\Omega\,\mathrm{cm}$. The substrate thickness is about 725(30) µm. An oxide is grown on top of the substrate by thermal oxidation. This oxide is relatively thick, of about 2 µm. The interdigital structure has been made of an aluminum-silicon alloy (silumin). This alloy is corrosion resistant, making the transducer more resilient to humid environment. A few nanometer titanium dioxide TiO_2 coating has been performed on top of the metal, noticeable on picture 4.2d. TiO_2 acts as a transparent heat reflector (THR) and protects the metal against heat radiation. Four different wafers have been produced:

- Wafer400 without passivation layer
- Wafer200
- Wafer400

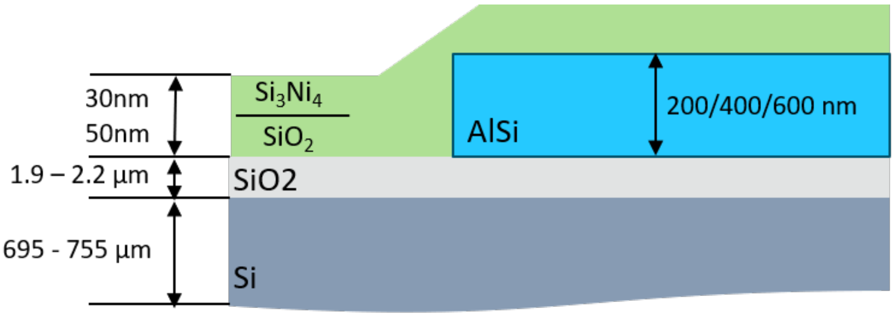

Figure 4.1: Cross-section schematic of the wafers.

- Wafer600

The number defining the wafer name represents the thickness, in nanometer, of the metal. The passivation layer is a SIO_2/Si_3N_4 thin double layer that has been coated on top of the entire wafer. Its thickness is about 50 nm/30 nm. A cross-section schematic is depicted on Fig. 4.1. Each wafer is made of 125 effective dies (Picture 4.2b). The two first columns are identical except for the probing pad via to the IDC, which is on top of the metal for the first one (see Fig. 4.2e) and buried for the second one. The third column contains differential IDC structures. In order to characterize the capacitance generated from an IDC, the first column will be analyzed. The different IDC parameters, for any wafer, are the following:

- $\eta = 0.5$
- L: 500 µm, 1000 µm
- W: 1 µm, 1.5 µm, 2 µm, 2.5 µm, 3 µm
- N: 11, 15, 19, 23, 27, 31, 35, 39, 43, 47

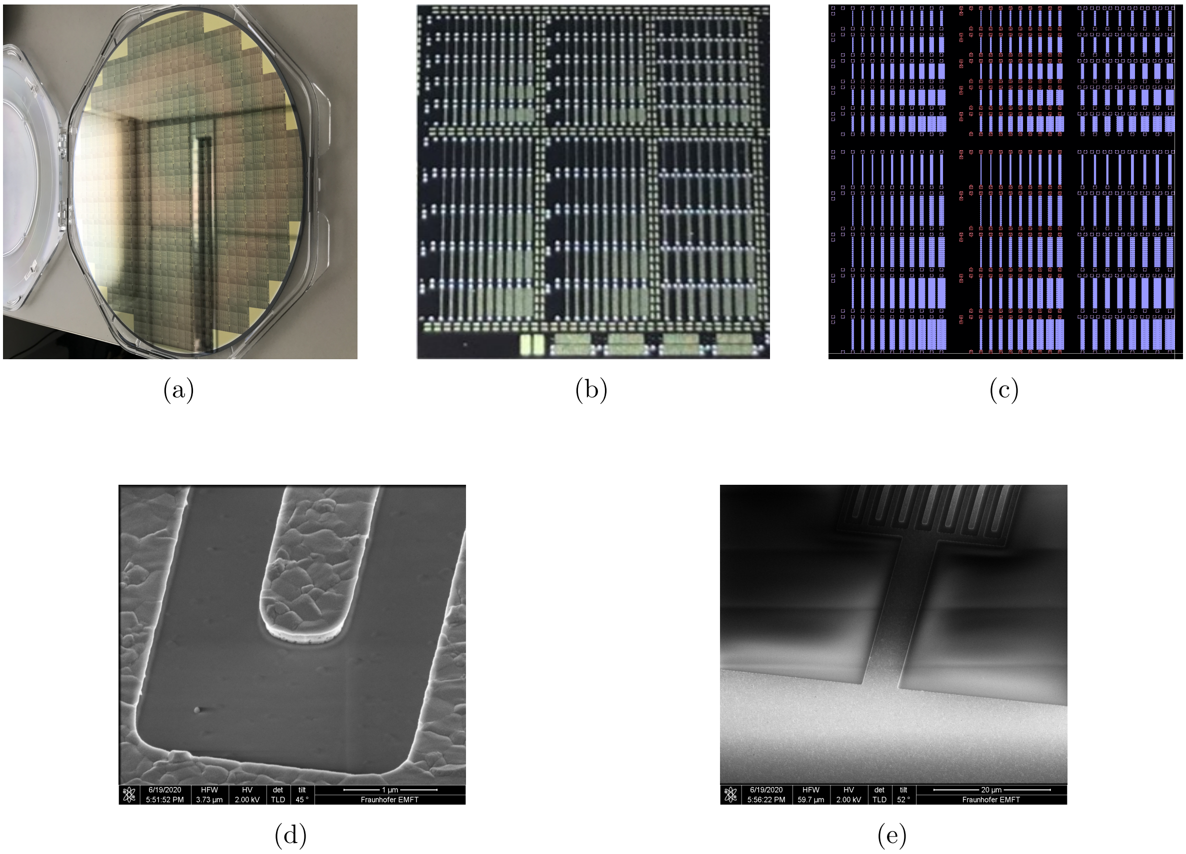

Figure 4.2: Pictures of the wafer600 (a), of a single die (b) and the corresponding layout (c). (a) Finger ending SEM picture taken from wafer400 without passivation layer. The TiO_2 is visible on top of the metal. (b) Probing pad to IDC metal via.

4.2 IDC structure On-Wafer characterization

The capacitance will be calculated with the Agilent 4294A precision impedance analyzer (Agilent Technologies, INC.) using the auto-balancing bridge method. The simplified diagram of the auto-balancing bridge circuit is depicted on Fig. 4.3. The testing protocole is a C-f routine. The frequency is swept from 1 kHz to 1 MHz. The high potential node is biased at $V_b = 1\,\mathrm{V}$ while the oscillation voltage is $V_{osc} = 250\,\mathrm{mV}$. The substrate is not grounded, in order to avoid the stray capacitance component, from the metal to the silicon. But this capacitance component has to be taken into account into the overall capacitance of the IDC since while on chip, the substrate is grounded. However, the auto-balancing bridge method, with the 2 probes on each side of the IDC, is not compatible with a grounded substrate, otherwise the stray capacitance will not be read out and a part of the fringe capacitance will vanish into the substrate.

The first analysis that has been performed is the analysis of the capacitance deviation on the wafer, closely related to the IDC parameters deviation. Fig. 4.4 identify the capacitance deviation along the wafers for a couple structures. One can notice the lower values of capacitance for the dies on the lower right center of the wafers. This deviation is correlated to the oxide thickness. The oxide layer is thicker at this point and decreases when closer to the edge. Indeed, a thinner oxide means a more important electric field density in the lower layer: the silicon substrate. As the silicon permittivity is higher than the silicon oxide one, it explains the lower values of capacitance for a thinner oxide. It is also interesting to notice circular interference patterns centered on the same spot and that can be seen on picture 4.2a. This patterns show the variation of oxide thickness. The light that is refracted then reflected in the oxide interferes with the part of the light that is only reflected on the surface.

Fig. 4.5 shows the capacitance for all the $L = 1\,\mathrm{mm}$ structures on the die 77 on Wafer400. One can notice the very good linearity of the capacitance with respect to the number of fingers.

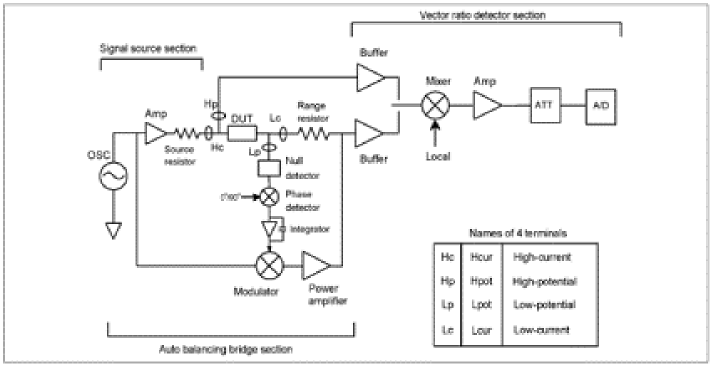

Figure 4.3: Auto-balancing bridge sensing circuit from Agilent 4294A precision impedence analyzer.

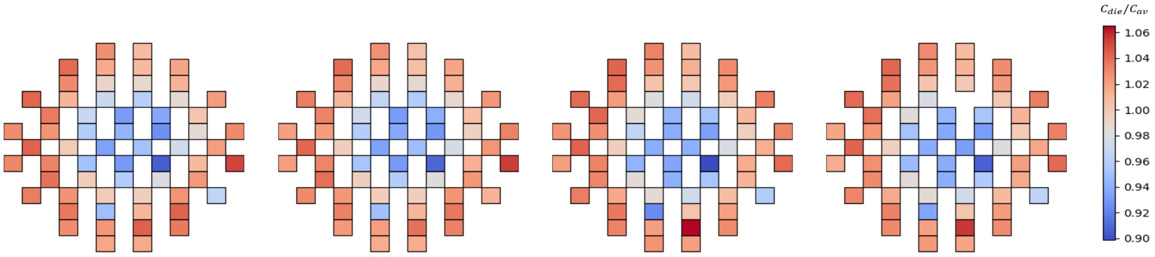

(a) Wafer200 L05_W10_N19 (b) Wafer200 L05_W10_N35 (c) Wafer200 L10_W10_N19 (d) Wafer200 L10_W10_N35

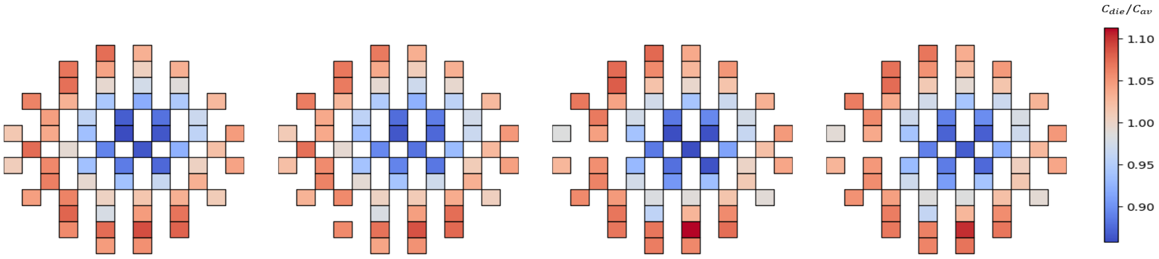

(e) Wafer400 L05_W10_N19 (f) Wafer400 L05_W10_N35 (g) Wafer400 L10_W10_N19 (h) Wafer400 L10_W10_N35

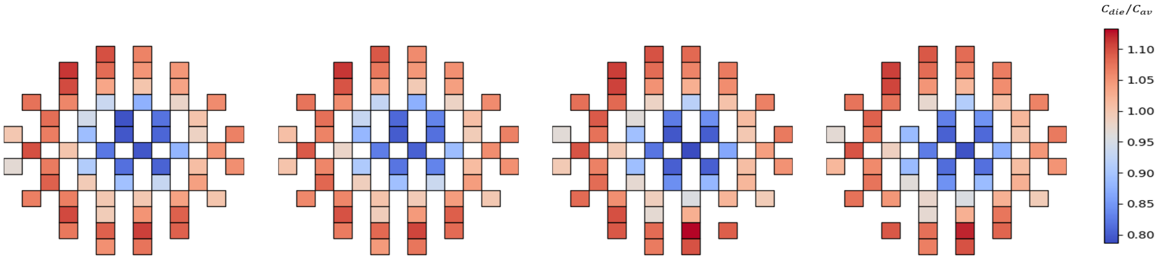

(i) Wafer600 L05_W10_N19 (j) Wafer600 L05_W10_N35 (k) Wafer600 L10_W10_N19 (l) Wafer600 L10_W10_N35

Figure 4.4: Wafer mapping of the value at 100 kHz C_{die}/C_{av} with C_{die} the value of the structure's capacitance corresponding die, and C_{av} the average capacitance of the same structure all over the wafer (from colored dies on the picture).

The capacitance also seems to decrease with the finger width. In order to compare the results with model and FEM, the model will be applied on this IDC structure.

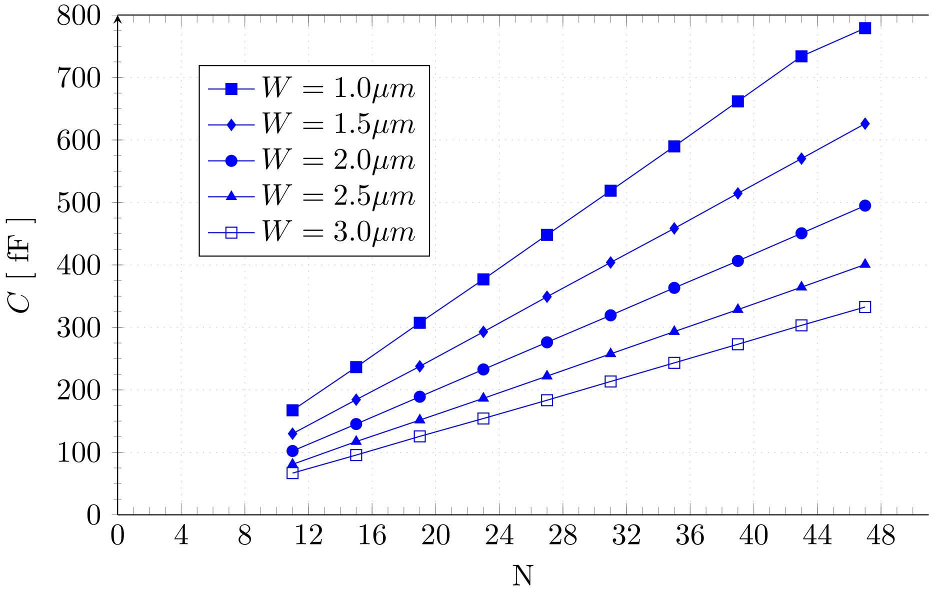

Figure 4.5: Capacitance values at 10 kHz on Wafer400 from die 77 with $L = 1\,\text{mm}$ for different finger's numbers and width.

For the capacitance model of this IDC, a SPC case will be considered for the bottom part with a SiO_2/Si double layer. For the upper part, it is very complicated to take the passivation layer into account. On the one hand because of the particular geometry (it is not a horizontal layer), and on the other hand, because for a three-layer model SiO_2/Si_3N_4/Air, the corresponding relative permittivities are 3.9/7.5/1, which does not correspond to a PPC or SPC case.

For the IDC L05_W10_N35 ($L = 500\,\mu\text{m}$, $W = 1\,\mu\text{m}$ and $N = 35$), the average relative increase of the capacitance due to the passivation layer is about 21%. This is expected to remain invariant to different length and number of finger, but decrease for large W. Indeed, for larger W, the capacitance from the passivation layer decreases, being highly related to the ratio $r = h/\lambda$ with h the thickness of the layer. In the meantime, the r ratio of the oxide decreases as well, and the capacitance issued from the silicon substrate, for which the permittivity is higher, substantially increase.

The IDC cells capacitance C_I and C_E are calculated from the upper and bottom parts as follow:

$$C_I = C_{IUP} + C_{IDW} \tag{4.1}$$

$$C_E = C_{EUP} + C_{EDW} \tag{4.2}$$

Where C_{IUP}, C_{IDW}, C_{EUP} and C_{EDW} are the interior and exterior, lower and upper cells capacitance. The upper plane is considered as a single infinite air layer. C_{IUP} and C_{EUP} are then calculated as follow:

$$C_{IUP} = C_I(\infty) \tag{4.3}$$

$$C_{EUP} = C_E(\infty) \tag{4.4}$$

The bottom configuration is a SPC case with a silicon oxide layer on top of a silicon substrate. Due to the conductivity of the p-doped silicon, its permittivity has a complex component also depending on the signal frequency. The silicon relative permittivity is written $\varepsilon^*_{Si} = \varepsilon_{Si} - j\frac{\sigma}{2\pi f \varepsilon_0}$, with σ the conductivity of the silicon, evaluated around $100\,\mathrm{S\,m^{-1}}$. From the SPC method, C_{IDW} and C_{EDW} are calculated as follow:

$$\frac{1}{C_{IDW}} = \left[\frac{1}{\varepsilon_{SiO_2}} - \frac{1}{\varepsilon^*_{Si}}\right]\frac{1}{C_I(h_{SiO_2})} + \frac{1}{\varepsilon^*_{Si}}\frac{1}{C_I(\infty)} \tag{4.5}$$

$$\frac{1}{C_{EDW}} = \left[\frac{1}{\varepsilon_{SiO_2}} - \frac{1}{\varepsilon^*_{Si}}\right]\frac{1}{C_E(h_{SiO_2})} + \frac{1}{\varepsilon^*_{Si}}\frac{1}{C_E(\infty)} \tag{4.6}$$

The total capacitance is then calculated with formula 2.4. The Fig. 4.6 shows the difference between the experimental data with FEM and model. The difference between numerical

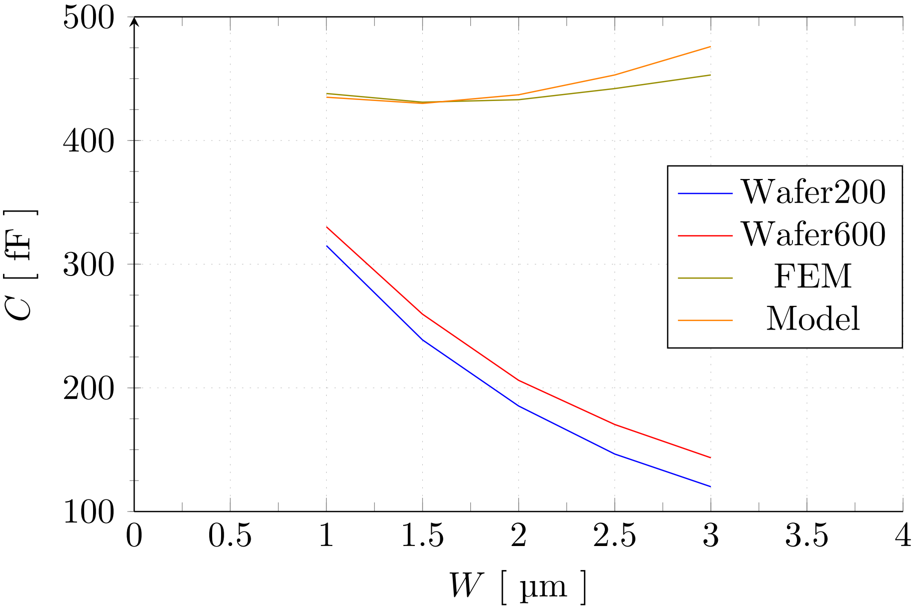

Figure 4.6: Capacitance behavior with respect to finger width W for structure L10_Wxx_N19 at 100 kHz. The FEM simulation has been performed in DC mode.

method and FEM for large fingers width is due to the fact that the simulation has been performed in DC mode. The complex component of the silicon permittivity is then neglected. Although, the experimental data are not as expected. Indeed, one expects the capacitance to increase for larger W, at constant η, with such SPC configuration. With larger fingers width, the electrical field density concentration in the substrate increases. Since it has a higher relative permittivity, the capacitive effect is enhanced. This behavior is generalized on all the wafers for any structure with respect to W (See Fig. 4.5).

In order to make sure that no depletion layers were formed into the substrate, the measurements have been performed with and without bias voltage but led to the same results. The oxide thickness being about 1.9 µm, the electric field density in the substrate for $W = 1\,\mu\text{m}$ and $\eta = 0.5$ is negligible, according to the model. The offset in between the first points lead to think that what have been simulated and modeled do not correspond to what the analyser is measuring.

5 Conclusion

In this work, some analytical descriptions of the IDC structure, namely Igreja model from [23] and [24], have been adapted to characterize the generated capacitance of a CMOS monolithic interdigital capacitive transducer for PM sensing. In a second part, the conformal mapping process, widely used in IDC analysis, has been detailed for PM mapping. Then a theory on the effect of ellipsoids in uniform electric fields has been adapted and used. Combined with conformal mapping, it has enabled the derivation of a numerical method to calculate the capacitance increment due to the presence of PM on the sensor. Such a model, extremely faster than usual FEM simulation, has a great value for design parametrisation.

Although, the limitations of this model are well defined, and enumerated in section 3.4. Although the accuracy of the model increases drastically for spherical objects that are smaller than the size of the electrode.

Even though the FEM simulation and the analytical models match with a good reliability, the results from experimental data were not expected. The mismatch for small fingers width and the behavior of the silicon substrate have not been unveiled so far.

As a conclusion and further development ideas, the analytical model for the PM capacitance shift is promising and can be developed further. For instance, mapping the space between two electrode halves, that is to say the $C_I/2$ capacitance section from Fig. 2.4, would shift away the boundaries of a sub-cell. It would result in a more accurate model for the same range of PM diameters, but also increase the range of diameters that can be mapped.

Bibliography

[1] E. G. e. a. Snyder, “The changing paradigm of air pollution monitoring”, *Environmental Science & Technology*, vol. 47, pp. 11 369–11 377, 20 2013. DOI: `10.1021/es4022602`.

[2] H. Nazemi, A. Joseph, J. Park, and A. Emadi, “Advanced micro- and nano-gas sensor technology: a review”, *Sensors (Basel)*, vol. 19, p. 1285, 6 2014. DOI: `10.3390/s19061285`.

[3] I. Contribution of Working Groups I and III, “Climate change 2007: synthesis report”, ipcc, Geneva, Switzerland, Tech. Rep., 2007.

[4] H. H. S. Mark J. Nieuwenhuijsen, “Exposure assessment in occupational and environmental epidemiology”, in. 2003, ch. Section II / 14: Particulate matter.

[5] P. A. Solomon, P. Gehr, D. H. Bennett, R. F. Phalen, L. B. Mèndez, B. Rothen-Rutishauser, M. Clift, C. Brandenberger, and C. Mählfeld, “Macroscopic to microscopic scales of particle dosimetry: from source to fate in the body”, *Air Quality, Atmosphere & Health*, vol. 5, pp. 169–187, 2012, ISSN: 1873-9326. DOI: `10.1007/s11869-011-0167-y`.

[6] D. Krewski, “Evaluating the effects of ambient air pollution on life expectancy”, *The New England Journal of Medicine*, vol. 360, no. 4, pp. 413–415, 2009. DOI: `10.1056/NEJMe0809178`.

[7] M. Kampa and E. Castanas, “Human health effects of air pollution”, *Environmental Pollution*, vol. 151, no. 2, pp. 362–367, 2008. DOI: `10.1016/j.envpol.2007.06.012`.

[8] C. Pope and D. Dockery, “Health effects of fine particulate air pollution: lines that connect”, *Journal of the Air and Waste Management Association*, vol. 56, no. 6, pp. 709–742, 2006, ISSN: 1047-3289.

[9] O. R.-N. et al, “Air pollution and lung cancer incidence in 17 european cohorts: prospective analyses from the european study of cohorts for air pollution effects (escape)”, *The Lancet Oncology*, vol. 14, pp. 813–822, 9 2013. DOI: `10.1016/S1470-2045(13)70279-1`.

[10] UNEP, *Climate Change 2001: Working Group 1.* 2001.

[11] F. J. Kelly, “Oxidative stress: its role in air pollution and adverse health effects”, *Occup Environ Med.*, vol. 60, pp. 612–616, 2003, ISSN: 1351-0711. DOI: `10.1136/oem.60.8.612`. [Online]. Available: `https://pubmed.ncbi.nlm.nih.gov/12883027`.

[12] S. Kundu and E. A. Stone, “Composition and sources of fine particulate matter across urban and rural sites in the midwestern united states”, *Environ. Sci.: Processes Impacts*, vol. 16, pp. 1360–1370, 6 2014. DOI: `10.1039/C3EM00719G`.

[13] W. H. Organization, “Health aspects of air pollution with particulate matter, ozone and nitrogen dioxide”, WHO, Tech. Rep., 2003, ch. 5, pp. 7–29.

[14] J. Stratton, *Electromagnetic Theory.* New York, USA: McGraw-Hill, 1941.

[15] M. Jovašević-Stovaiović, A. Bartonova, D. Topalović, I. Lazović, B. Pokrić, and Z. Ristovski, “On the use of small and cheaper sensor and devices for indicative citizen-based monitoring of respirable particulate matter”, *Environmental Pollution*, vol. 206, pp. 696–704, 2015. DOI: `10.1016/j.envpol.2015.08.035`.

[16] I. Paprotny, F. Doering, P. Solomon, R. White, and L. Gundel, “Microfabricated air-microfluidic sensor for personal monitoring of airborne particulate matter: design, fabrication, and experimental results”, *Sensors and Actuators A: Physical*, vol. 201, pp. 506–516, Oct. 2013. DOI: `10.1016/j.sna.2012.12.026`.

[17] N. Ngo, J. Lee, M.-W. Kim, and J. Jang, “Measurement of pm 2.5 mass concentration using an electrostatic particle concentrator-based quartz crystal microbalance”, *IEEE Access*, vol. 7, pp. 170 640–170 647, Jan. 2019. DOI: `10.1109/ACCESS.2019.2955377`.

[18] P. Ciccarella, M. Carminati, M. Sampietro, and G. Ferrari, “Multichannel 65 zf rms resolution cmos monolithic capacitive sensor for counting single micrometer-sized airborne particles on chip”, *IEEE Journal of Solid-State Circuits*, vol. 51, no. 11, pp. 2545–2553, 2016.

[19] J. W. Brown and R. V. Churchill, *Complex Variables and Applications. Eighth Edition.* New York, USA: McGraw-Hill, 2008.

[20] J. Wei, “Distributed capacitance of planar electrodes in optic and acoustic surface wave devices”, *IEEE Journal of Quantum Electronics*, vol. 13, no. 4, pp. 152–158, 1977.

[21] Huey-Daw Wu, Zhihang Zhang, F. Barnes, C. M. Jackson, A. Kain, and J. D. Cuchiaro, “Voltage tunable capacitors using high temperature superconductors and ferroelectrics”, *IEEE Transactions on Applied Superconductivity*, vol. 4, no. 3, pp. 156–160, 1994.

[22] S. S. Gevorgian, T. Martinsson, P. L. J. Linner, and E. L. Kollberg, “Cad models for multilayered substrate interdigital capacitors”, *IEEE Transactions on Microwave Theory and Techniques*, vol. 44, no. 6, pp. 896–904, 1996.

[23] R. Igreja and C. Dias, “Analytical evaluation of the interdigital electrodes capacitance for a multi-layered structure”, *Sensors and Actuators A*, vol. 112, no. 2-3, pp. 291–301, 2004.

[24] ——, “Extension to the analytical model of the interdigital electrodes capacitance for a multi-layered structure”, *Sensors and Actuators A*, vol. 172, no. 2, pp. 392–399, 2011.

[25] Y. Feng, J. Hallstedt, Q. Chen, L. Zheng, and Y. Huang, “Development and experimental verification of analytical models for printable interdigital capacitor sensors on paperboard”, in *SENSORS, 2009 IEEE*, 2009, pp. 1034–1039.

[26] N. H. Zhu, E. Y. B. Pun, and J. X. Li, "Analytical formulas for calculating the effective dielectric constants of coplanar lines for oic applications", *Microwave and Optical Technology Letters*, vol. 9, no. 4, pp. 229–232, 1995. DOI: `10.1002/mop.4650090419`.

[27] G. Ghione and M. Goano, "Revisiting the partial-capacitance approach to the analysis of coplanar transmission lines on multilayered substrates", *IEEE Transactions on Microwave Theory and Techniques*, vol. 51, no. 9, pp. 2007–2014, 2003.

[28] M. Abramowitz and S. I.A., *Handbook of Mathematical Functions with Formulas, Graphs, and Mathematical Tables*. New York, USA: Dover, 1970.

[29] H. A. Wheeler, "Transmission-line properties of parallel strips separated by a dielectric sheet", *IEEE Transactions on Microwave Theory and Techniques*, vol. 13, no. 2, pp. 172–185, 1965.

[30] S. Giordano, "Effective medium theory for dispersions of dielectric ellipsoids", *Journal of Electrostatics*, vol. 58, pp. 59–76, May 2003. DOI: `10.1016/S0304-3886(02)00199-7`.

[31] J. Virbalis and S. Å½ebrauskas, "The influence of dielectric admixtures on capacitance of plane capacitor", *Elektronika ir Elektrotechnika*, Jan. 2007.

[32] J. A. Osborn, "Demagnetizing factors of the general ellipsoid", *Phys. Rev.*, vol. 67, pp. 351–357, 11-12 1945. DOI: `10.1103/PhysRev.67.351`.